Contents lists available at ScienceDirect

Chemical Geology

Fluid origin and critical ore-forming processes for the giant gold mineralization in the Jiaodong Peninsula, China: Constraints from in situ elemental and oxygen isotopic compositions of quartz and LA–ICP–MS analysis of fluid inclusions

Hong Wang [a,b], Ting-Guang Lan [a,b,*], Hong-Rui Fan [c], Zhi-Long Huang [a], Huan-Long Hu [a], Ying-Hua Chen [a,b], Yan-Wen Tang [a], Jiao Li [c]

[a] *State Key Laboratory of Ore Deposit Geochemistry, Institute of Geochemistry, Chinese Academy of Sciences, Guiyang 550081, China*
[b] *College of Earth and Planetary Sciences, University of Chinese Academy of Sciences, Beijing 100049, China*
[c] *Institute of Geology and Geophysics, Chinese Academy of Sciences, Beijing 100029, China*

ARTICLE INFO

ABSTRACT

The Jiaodong Peninsula, China, is one of the largest gold provinces in the world. During a short time interval in the Early Cretaceous, over 5000 t of gold were accumulated there. The mechanisms controlling the focused Au deposition and the origins of massive amounts of auriferous fluids are still controversial. Quartz–sulfide lode mineralization (Linglong-type) and disseminated/stockwork mineralization (Jiaojia-type) are the two major mineralization styles in the Jiaodong Peninsula. Herein, we conducted in situ textural, elemental and oxygen isotopic analyses using scanning electron microscopy (SEM), laser ablation-inductively coupled plasma-mass spectrometry (LA–ICP–MS) and secondary ion mass spectrometry (SIMS) on quartz from different hydrothermal stages and depths for three representative Linglong-type (Linglong deposit) and Jiaojia-type (Xiadian and Jiangjiayao deposits) gold deposits in the northwestern Jiaodong Peninsula, with the aim to constrain the ore-forming processes. The LA–ICP–MS analysis of individual fluid inclusions was also conducted to unravel the origin of the auriferous fluids. The results show that from the pre-mineralization to the ore-forming stages in the Linglong-type mineralization, the homogenization temperatures and salinities of fluid inclusions and the $\delta^{18}O_{quartz}$ values change slightly, but the Al concentrations of quartz decrease continuously. Combined with the coexistence of CO_2- and H_2O-rich fluid inclusion endmembers, these trends indicate the increase of pH induced by CO_2 degassing (fluid–fluid unmixing), which led to focused Au deposition. The quartz grains from the Jiaojia-type mineralization typically show a homogeneous texture with well-correlated lithophile elements (e.g., K, Al and Rb), which are distinct from those of the Linglong-type that are characterized by oscillatory zoning with much higher Al concentrations and $\delta^{18}O_{quartz}$ values. These phenomena indicate that enhanced fluid–rock interaction occurred in the Jiaojia-type mineralization. In addition, the $\delta^{18}O_{quartz}$ values show an increase from deep to shallow depths. In combination with thermodynamic modelling, it suggests decreasing fluid–rock interaction with decreasing depth. The above results corroborate that multiple mechanisms led to the efficient Au deposition in the Jiaodong Peninsula. Fluid–fluid unmixing typically occurred in the Linglong-type mineralization, while fluid–rock interaction was dominant in the Jiaojia-type mineralization. The different mechanisms might render mining challenging due to the changeable locations of favorable Au unloading.

The LA–ICP–MS results of fluid inclusions suggest that the ore-forming fluids are metamorphic fluids rather than magmatic–hydrothermal fluids. In combination with the isotopic compositions of ores showing considerable mantle affinities and large-scale mafic underplating occurring beneath the study region, we propose a new genetic model that accounts for the origin of the auriferous fluids. The new model invokes the devolatilization of previously emplaced H_2O- and Au-rich amphibole cumulates through amphibolite- to granulite-facies metamorphism in the middle–lower crust. It suggests an alternative way to generate the 'orogenic-like' gold deposits.

---

1. Introduction

The Jiaodong Peninsula is the largest gold province in China (Fig. 1), which hosts over 100 gold deposits with more than 5000 t of gold within an area of less than 30,000 km^2 (Deng et al., 2020). The gold deposits are fault-controlled, most of which occur along the NE- to NEE-trending faults. All kinds of dating methods (e.g., K—Ar, $^{40}Ar/^{39}Ar$, Rb—Sr, Re—Os and U—Pb dating) show that the gold deposits formed at 120 ± 2 Ma (Zhang et al., 2020 and references therein), being 10–40 Ma younger than their host granitoids or 1.8 Ga later than the metamorphism of their host metamorphic rocks. They have uniform H_2O + NaCl + CO_2 ± CH_4 fluid inclusions that show high CO_2 contents (mainly 10–20 mol%), low salinities (commonly <10 wt% NaCl$_{eqv.}$) and moderate to low homogenization temperatures (mainly 200 °C–350 °C) (Qiu et al., 2002; Fan et al., 2007; Li et al., 2015). Two distinct mineralization styles have been identified, namely the Linglong-type and the Jiaojia-type. The former is characterized by quartz–sulfide lode mineralization while the latter is characterized by disseminated and stockwork mineralization (Qiu et al., 2002). Microthermometric results show that the salinities and homogeneous temperatures of fluid inclusions change insignificantly either from the early to the late ore-forming stages or from the deep to the shallow depths or between the different mineralization styles (e.g., Wen et al., 2015, 2016; Guo et al., 2017; Liu et al., 2018). In addition, the isotopic compositions (e.g., C—O, S, Sr-Nd-Pb and He—Ar) of ores commonly show transitional features between the crustal and mantle-derived rocks (Mao et al., 2008; Li and Santosh, 2014; Li et al., 2015; Deng et al., 2020). These results lead to a variety of fluids to be proposed as the ore-forming fluids, including magmatic–hydrothermal fluids derived from crustal reworking (e.g. Wang et al., 1989; Yan et al., 2014; Xiong et al., 2020), mantle fluids derived from mantle melting or degassing (e.g. Mao et al., 2008; Deng et al., 2020; Wang et al., 2020) and dehydration fluids from oceanic slab (e.g. Goldfarb and Santosh, 2014; Groves and Santosh, 2016; Zhu and Sun, 2021). To exactly constrain the origin of the auriferous fluids and the ore-forming processes, detailed investigations on the temporal and spatial variations of the ore-forming fluids are required.

Fluid inclusions can provide the direct information about the ore-forming fluids, especially when analyzed using LA–ICP–MS (Heinrich et al., 2003; Pettke et al., 2012; Wagner et al., 2016). Quartz is the major host mineral of fluid inclusions and gangue mineral in magmatic–hydrothermal ore deposits. Its geochemistry has been widely used to trace the ore-forming processes (e.g. Allan and Yardley, 2007; Rusk et al., 2008; Kerr et al., 2018; Rottier et al., 2021). Herein, combining the in situ analyses of SEM, LA–ICP–MS and SIMS, we conducted integrated textural, elemental and isotopic studies on quartz from different hydrothermal stages, depths (altitudes between −10 m and − 1600 m) and mineralization styles (Linglong-type and Jiaojia-type) for three representative gold deposits (Linglong, Xiadian and Jiangjiayao deposits) in the northwestern Jiaodong Peninsula. The LA–ICP–MS analysis of fluid inclusions was also conducted for the first time for the Jiaodong gold deposits. Our studies shed new light on the origin of the auriferous fluids and provide new insights into how Au was deposited in different structural settings.
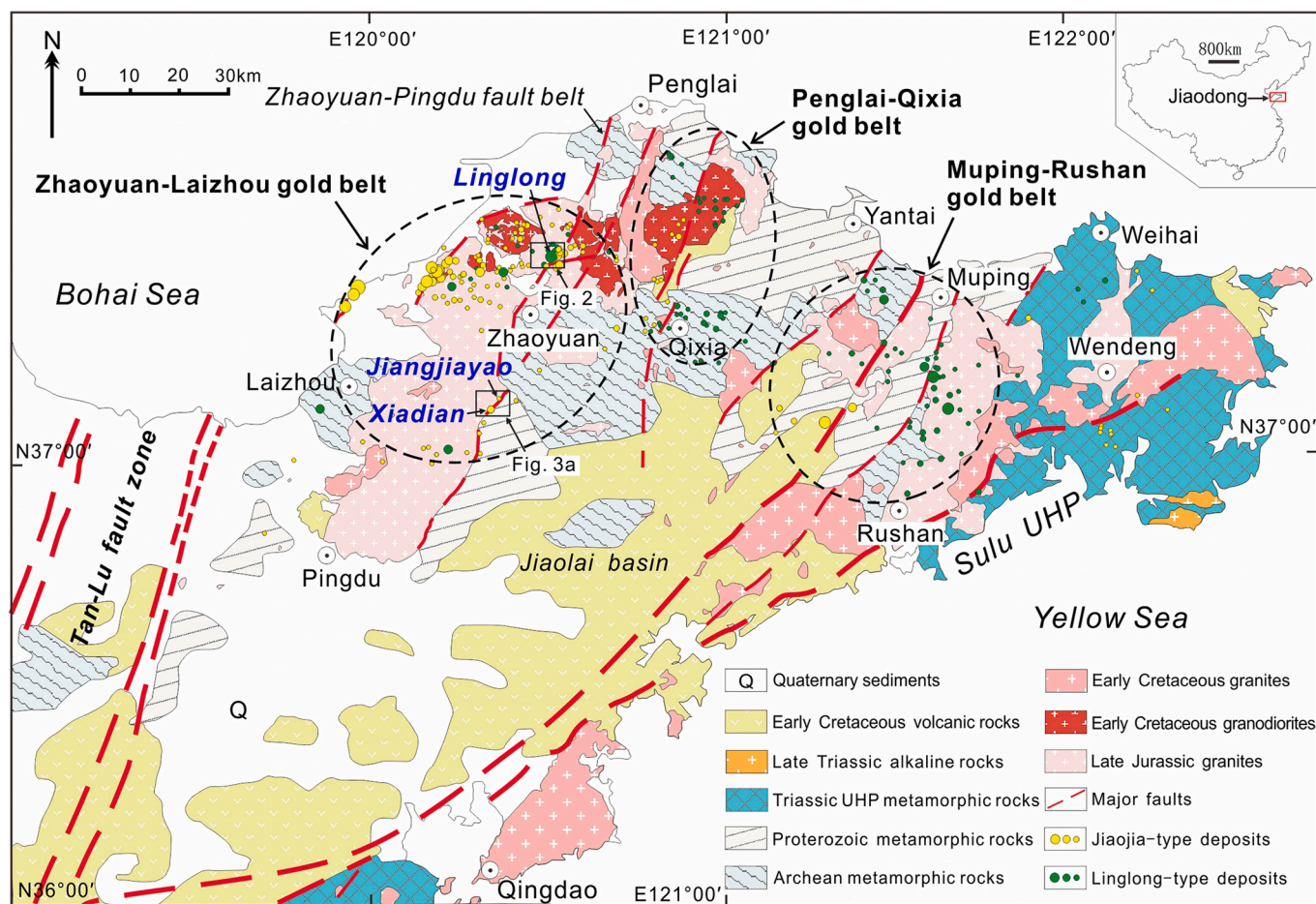

Fig. 1. Regional geologic map of the Jiaodong Peninsula and the distribution of gold deposits (modified after Wen et al., 2016). (For interpretation of the references to colour in this figure legend, the reader is referred to the web version of this article.)

2. Geological setting

2.1. Regional geology

The Jiaodong Peninsula is located at the eastern margin of the North China Craton (NCC), eastern China (Fig. 1). It is mainly composed of Archean (2.9–2.5 Ga) to Paleoproterozoic (2.3–2.0 Ga) trondhjemite–tonalite–granodiorite (TTG) gneisses, meta-volcanic and meta-sedimentary rocks, Late Triassic (240–225 Ma) ultrahigh- to high-pressure metamorphic rocks, Late Jurassic (160–150 Ma) granites and Early Cretaceous (130–93 Ma) granitoids and volcanic rocks (Goldfarb and Santosh, 2014; Deng et al., 2020). Early Cretaceous (131–110 Ma) mafic to felsic dykes are also widespread in the Jiaodong Peninsula (Deng et al., 2017). Three major gold belts have been identified, which are termed the Zhaoyuan–Laizhou, Penglai–Qixia and Muping–Rushan belts from west to east (Fig. 1). These gold belts comprise a series of NE- to NNE-trending faults, along which the gold deposits are distributed. The gold deposits are mainly hosted in the Mesozoic granitoids with some in the Precambrian metamorphic rocks (Fig. 1). Gold mineralization occurs either as Au-bearing quartz–sulfide lodes or as disseminations and stockworks in altered rocks, which are called the Linglong-type and Jiaojia-type mineralization, respectively (Qiu et al., 2002). The two styles of mineralization cannot be distinguished by wallrocks,

alteration types and fluid inclusions (Wen et al., 2015; Guo et al., 2017), but can differ in structural settings. The Linglong-type mineralization occurs in the lower-order, steeply-dipping (>60°) fractures distal to the regional main faults, while the Jiaojia-type occurs in the less steep (<45°) fractures close to the main faults (Qiu et al., 2002; Li et al., 2015).

The Zhaoyuan–Laizhou gold belt is the most important gold belt, hosting over 80% of the known Au reserves in the Jiaodong Peninsula. The Zhaoyuan–Pingdu fault is one of the major gold-hosting faults in this belt, within which both the Linglong- and Jiaojia-type mineralization styles occur (Fig. 1). The coexistence of the two distinct mineralization styles makes this fault an excellent region for studying how Au was transported and deposited in different structural settings. Representative gold deposits of the Linglong-type (Linglong deposit; Fig. 2) and Jiaojia-type (Xiadian and Jiangjiayao deposits; Fig. 3) mineralization from this fault were selected for comparative studies.

2.2. Deposit geology of Linglong gold deposit

The Linglong gold deposit (also called the Linglong goldfield) is one of the most famous gold deposits in the Jiaodong Peninsula, hosting over 150 t of Au (predicted>500 t) (Qiu et al., 2002; Wen et al., 2015). This deposit comprises several mining areas (e.g., Xishan, Dongshan,
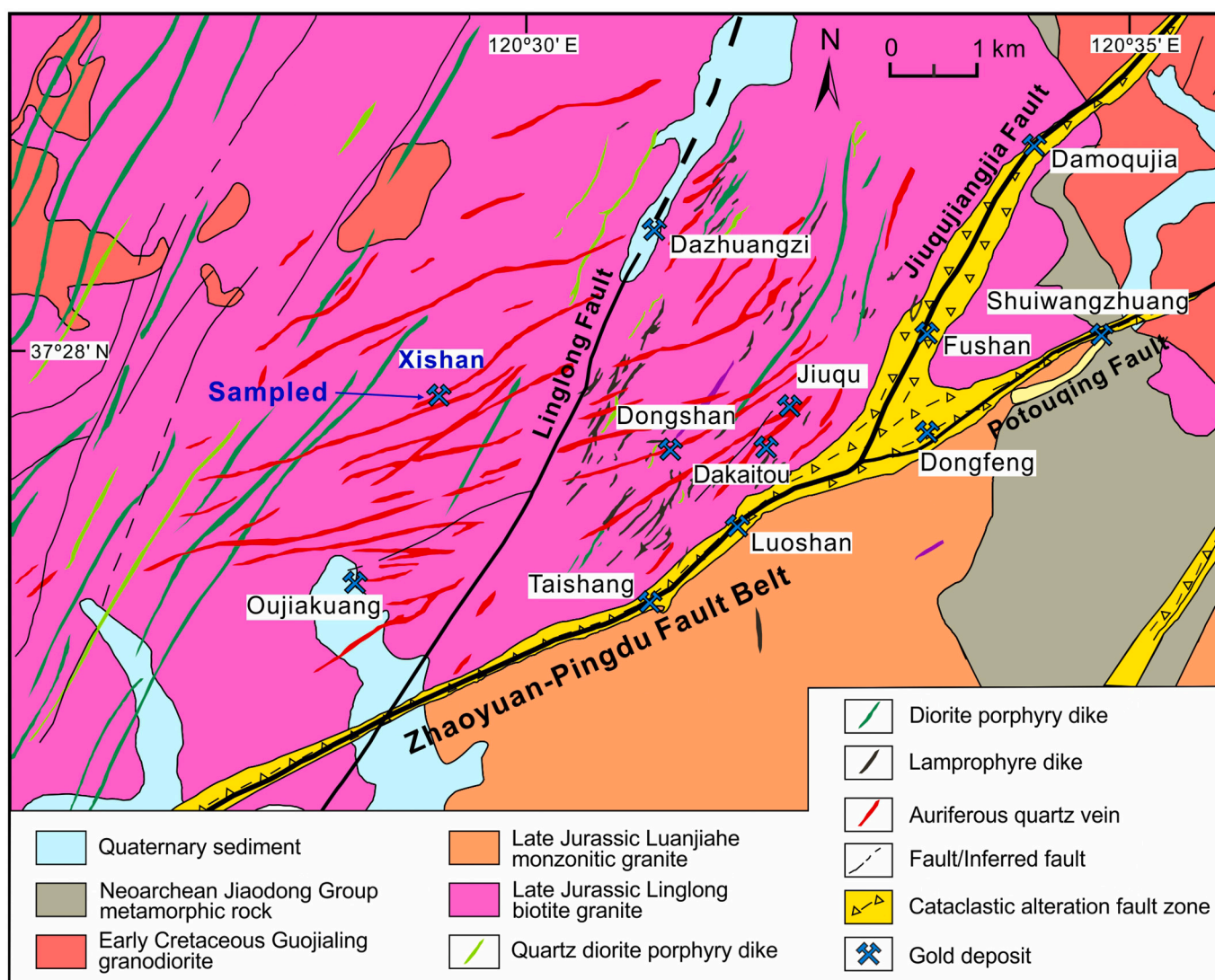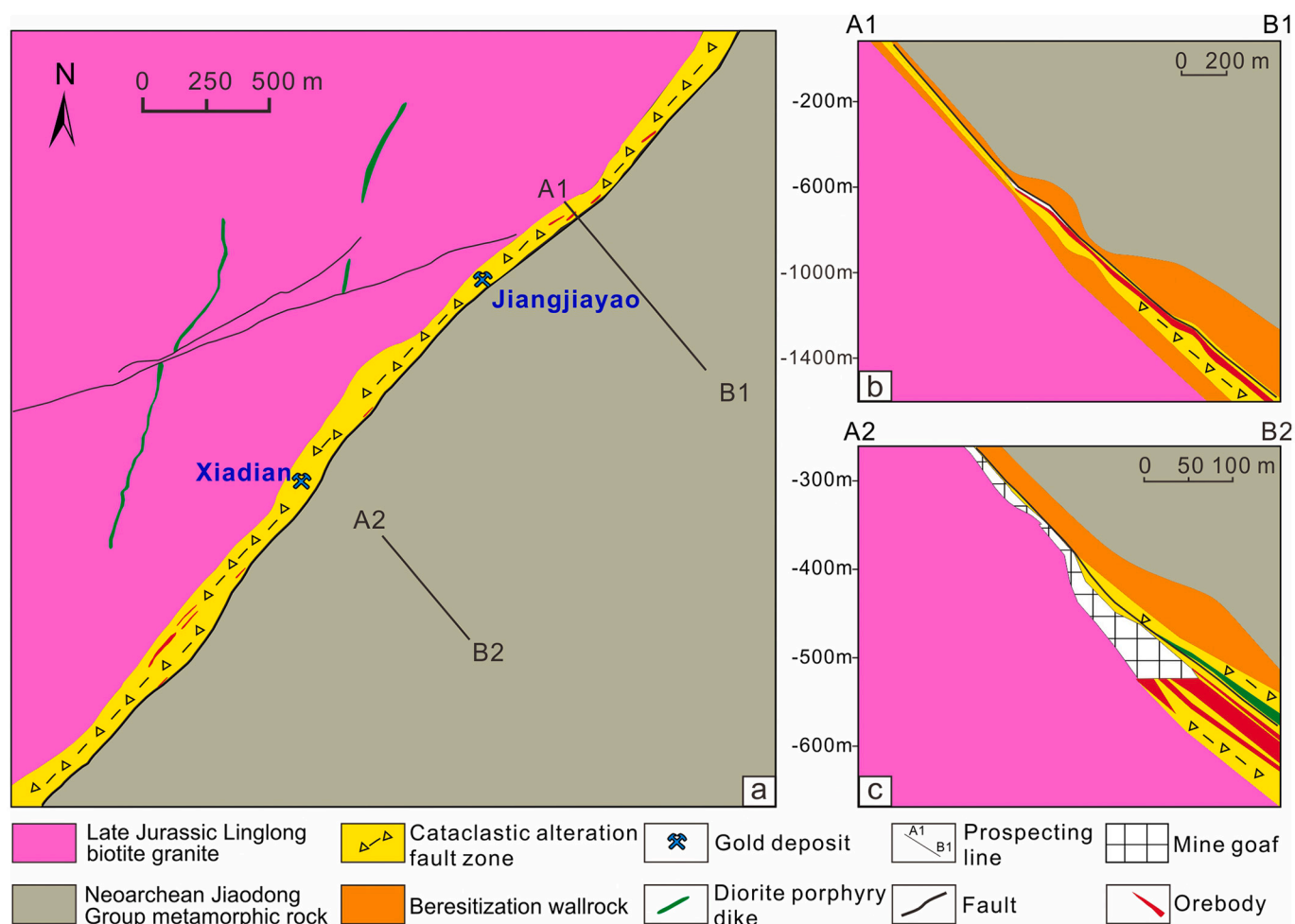

Fig. 2. Simplified geologic map of the Linglong goldfield (modified after Guo et al., 2017).

Fig. 3. Simplified geologic map (a) and geologic section of orebodies (b–c) for the Jiangjiayao and Xiadian gold deposits. (For interpretation of the references to colour in this figure legend, the reader is referred to the web version of this article.)

Dakaitou, Jiuqu, Shuangding, Oujiakuang, Taishang, Dongfeng and Luoshan areas), which contain over 200 ore veins (Fig. 2). The ore veins occur along the secondary faults of the Zhaoyuan–Pingdu fault and are roughly parallel to each other. They are mainly hosted in the Late Jurassic granites (~160 Ma), with few of them found in the Early Cretaceous granodiorites (~130 Ma). The ore veins are 0.5–10 m in width, 100–5500 m in length and + 600 to −1000 m in depth with NE to NNE strikes and NW 50°–80° dips (Fig. 4a). The Au grades vary from several to hundreds of g/t, with an average of 5–8 g/t.

Hydrothermal alterations are ubiquitous in the Linglong gold deposit, mainly including K-feldspathization, sericitization, silicification and sulfidation, which commonly show inward zoning from the wallrocks to the orebodies with the sequence of K-feldspathization→silicification/sericitization→sulfidation. Based on the cross-cutting relationships of hydrothermal veins and the mineral assemblages, four major hydrothermal stages can be identified: (I) the pre-mineralization quartz–K-feldspar stage (Fig. 4b), (II) the Au-bearing quartz–pyrite stage (Fig. 4c), (III) the Au-bearing quartz–polymetallic sulfide (e.g., chalcopyrite, galena, sphalerite and pyrrhotite) stage (Fig. 4d) and (IV) the post-mineralization quartz–carbonate stage (Fig. 4e). These hydrothermal stages are universal in the Jiaodong gold deposits, of which the stages II and III are the ore-forming stages. Gold mainly occurs as μm-scale visible grains in pyrite (Fig. 5a–d).

### 2.3. Deposit geology of Xiadian and Jiangjiayao gold deposits

The Xiadian and Jiangjiayao gold deposits are located 20–25 km

south of the Linglong gold deposit. They show similar geological features and host ~83 and ~ 26 t of Au, respectively. The two deposits are mainly situated at the contact zones between the Late Archean metamorphic rocks (hangingwall) and the Late Jurassic granites (footwall) along the regional Zhaoyuan–Pingdu fault plane (Fig. 3a). From the hangingwall to the footwall, the rocks show a zoning of potassic–sericitic metamorphic rocks→fault gouges→cataclastic beresites or beresitized granites (orebodies) → potassic–sericitic granites (Fig. 3b and c). The hydrothermal alterations are generally consistent with those in the Linglong gold deposit but show an enhanced superposition of different hydrothermal stages. The orebodies are 1–10 m in width, 20–500 m in length and + 160 to −600 m in depth, with NE 28–50° strikes and SE 42–51° dips. The Au grades vary from 1 to 55 g/t, with an average of 4–9 g/t. Both disseminated sulfides and quartz–sulfide stockworks are developed in the orebodies (Fig. 4f and g), where gold mainly occurs as μm-scale visible grains in sulfides (Fig. 5e and f).

3. Sampling and analytical methods

3.1. Sampling

Quartz ± sulfide veins of different hydrothermal stages (I, II, III and IV) are well developed in the Linglong gold deposit, samples of which were systematically collected to study the temporal evolution of the ore-forming fluids. Twenty-five samples were collected from the mining tunnels of the Xishan mining area at depths of −10 m to −50 m. Hydrothermal veins or lodes are poorly developed in the Xiadian and
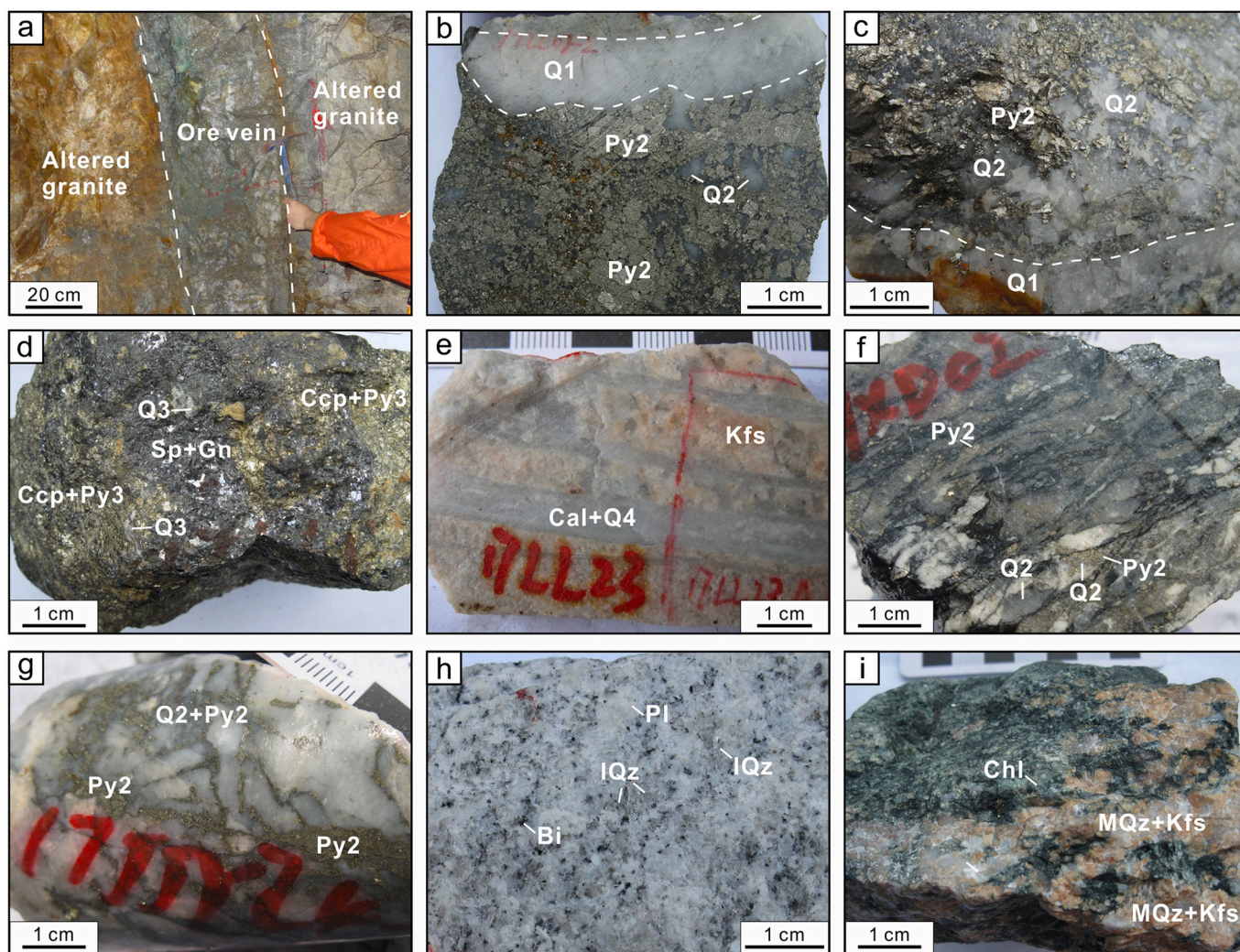
Fig. 4. Photographs of ores and wallrocks from the Linglong (a–e, h), Xiadian (f, i) and Jiangjiayao (g) gold deposits. (a) Au-bearing quartz + pyrite vein in altered granite, showing the Linglong-type mineralization. (b) Hydrothermal vein of stage I, cut by stage II. (c) Ore of hydrothermal stage II. (d) Ore of hydrothermal stage III. (e) Carbonate + quartz veinlets of hydrothermal stage IV. (f) Jiaojia-type disseminated mineralization in cataclastic rock. (g) Jiaojia-type stockwork mineralization in altered granite. (h) Late Jurassic biotite granite. (i) Quartz–K-feldspar pegmatitic veins in Late Archean gneiss. The Q1, Q2, Q3 and Q4 represent the quartz of the hydrothermal stage I, II, III and IV, respectively. Abbreviations: Py = pyrite; Ccp = chalcopyrite; Sp = sphalerite; Gn = galena; Q = quartz; IQz = igneous quartz; MQz = metamorphic quartz Bi = biotite; Pl = plagioclase; Kfs = K-feldspar; Cal = calcite; Chl = chlorite. (For interpretation of the references to colour in this figure legend, the reader is referred to the web version of this article.)

Jiangjiayao deposits, but stage II Au-bearing quartz–pyrite veinlets can be well identified and thus were sampled. Twenty-six samples from the Xiadian deposit were collected from the mining tunnels at depths of −450 m to −652 m. Thirty-four samples from the Jiangjiayao deposit were collected from drill core (ZK5) at depths of −1500 m to −1600 m. These samples facilitate to compare the spatial variations of the ore-forming processes. Fresh samples of the Late Jurassic granite (Fig. 4h) and quartz–K-feldspar veins within the Late Archean gneiss (Fig. 4i) were also collected for comparative studies among the igneous, meta-morphic and hydrothermal quartz. The detailed descriptions of the analyzed samples are listed in Table 1.

The rock samples were prepared into doubly polished thin sections for SEM, microthermometry, LA–ICP–MS and SIMS analyses. Fluid inclusion studies were conducted for the Lionglong deposit but not for the Xiadian and Jiangjiayao deposits owing to the small sizes of fluid inclusions (commonly <5 μm in diameter) in the latter two deposits. Except for the SIMS analysis, all the other analyses were conducted at the State Key Laboratory of Ore Deposit Geochemistry, Institute of Geochemistry, Chinese Academy of Sciences, Guiyang, China.

3.2. SEM-CL analysis of quartz

Scanning electron microscope cathodoluminescence (SEM-CL) observations of quartz veins were conducted using a JEOL JSM-7800F SEM equipped with an EDAX TEAM Apollo XL energy-dispersive X-ray spectrometry and a Gatan MonoCL4 cathodoluminescence detector. The working conditions of the SEM-CL imaging were an accelerating voltage of 10 kV and a beam current of 14 to 15 nA.

3.3. Laser Raman spectrometry of fluid inclusions

Laser Raman spectroscopic analysis of fluid inclusions was conducted using a LabRAM HR Evolution Raman spectrometer. An argon ion laser with a wavelength of 532 nm and a source power of 25 mW was used. The laser spot was ~2 μm in diameter. The Raman spectra were acquired in the range of 100–4000 cm^{-1} with an acquisition time of ~60 s for each analysis.
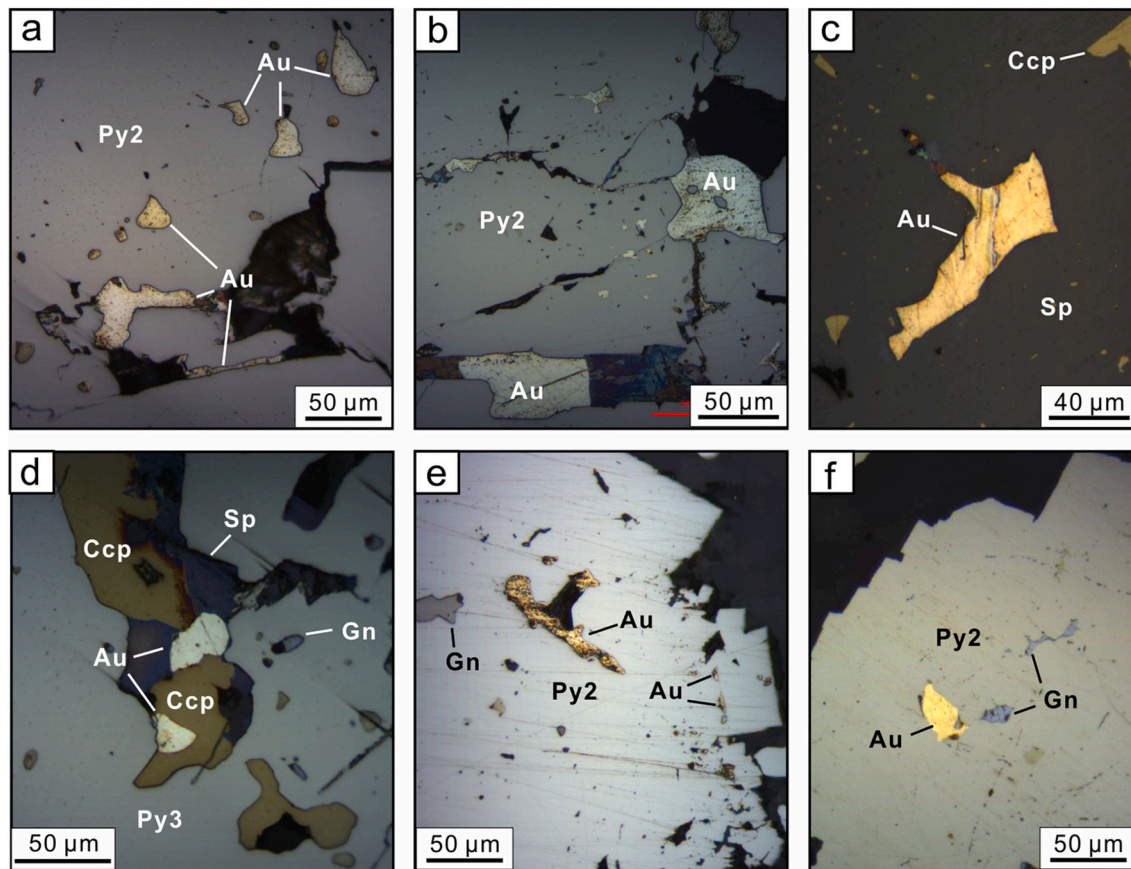
Fig. 5. Microphotographs of visible gold grains in sulfides (under reflected light) from the Linglong (a–d), Xiadian (e) and Jiangjiayao (f) gold deposits. (a, b) Gold grains occur as inclusions or in the fractures of pyrite from the hydrothermal stage II. (c, d) Gold grains in sulfides from the hydrothermal stage III. (e) Gold grains in pyrite from disseminated mineralization. (f) Gold grains in pyrite from stockwork mineralization. Abbreviations: Au = gold; Py = pyrite; Ccp = chalcopyrite; Gn = galena; Sp = sphalerite; Qz = quartz. (For interpretation of the references to colour in this figure legend, the reader is referred to the web version of this article.)

Table 1
Locations and descriptions of the samples selected for quartz and fluid inclusion studies.

Location	Altitude (m)	Hydrothermal stage	Description	LA-ICP-MS elemental analysis of quartz	SIMS $\delta^{18}O$ analysis of quartz	Fluid inclusion studies
Linglong deposit	−50	Stage I	Gold-barren Qz ± Kfs ± Py veins, commonly superposing on granitic wallrocks or cut by deuteric quartz ± sulfide veinlets; Qz is milky and coarse-grained with euhedral to subhedral shapes	17LL07–1A, 17LL10–1B	17LL07–1A	17LL01B, 17LL05–1, 17LL07–1A, 17LL09B, 17LL09C,
	−50	Stage II	Gold-bearing Qz–Py veins; Qz is white to smoky-gray and coarse- to fine-grained with euhedral to subhedral shapes	17LL01A, 17LL09C	17LL07	17LL01A, 17LL01B
	−10	Stage III	Gold-bearing quartz + polymetallic sulfide veins; Qz grains commonly show euhedral shapes	17LL10–1B, 17LL13B	17LL13B	17LL13A, 17LL13B, 17LL13C
	−10	Stage IV	Qz–Cal veinlets cutting preexisting mineral assemblages; Qtz grains are commonly subhedral to anhedral and fine-grained	17LL15A, 17LL21, 17LL23A	17LL15B, 17LL23A	17LL15A, 17LL15B, 17LL23A
	−10	Wallrock	Late Jurassic biotite granite, containing Qz–Pl–Kfs–Bi assemblages; Igneous Qz	17LL03, 17LL23B	17LL23B	
Xiadian deposit	−450	Stage II	Disseminated Py–Ser–Qz ores; Anhedral Qz	17XD16		
	−525	Stage II	Disseminated Py–Ser–Qz ores; Anhedral Qz	17XD12	17XD12	
	−525	Stage II	Stockwork Qz–Py veins; Anhedral Qz	17XD11B	17XD11B	
	−652	Stage II	Stockwork Qz–Py veins; Anhedral Qz	17XD06		
	−652	Stage II	Disseminated Py–Ser–Qz ores; Anhedral Qz	17XD02		
	−652	Wallrock	Qz–Kfs pegmatitic veins within late Archean gneiss; Metamorphic Qz	17XD01	17XD01	
Jiangjiayao deposit	−1512	Stage II	Stockwork Qz–Py veins; Anhedral Qz	17JJY07	17JJY07	
	−1513	Stage II	Stockwork Qz–Py veins; Anhedral Qz	17JJY10		
	−1529	Stage II	Stockwork Qz–Py veins; Anhedral Qz	17JJY15		
	−1565	Stage II	Stockwork Qz–Py veins; Anhedral Qz	17JJY24–1, 17JJY24–2	17JJY24–1	

Notes: Multiple generations of quartz or fluid inclusions can occur in one sample, which were commonly analyzed using the same thin section for different hydrothermal stages. Abbreviations: Py = pyrite; Qz = quartz; Kfs = K-feldspar; Pl = plagioclase; Bi = biotite; Cal = calcite; Ser = sericite.

3.4. Microthermometry of fluid inclusions

Microthermometric measurements of fluid inclusions were conducted with a Linkam THMSG 600 programmable heating–freezing stage equipped with an Olympus microscope. Calibrations against the triple-point of pure CO_2 (−56.6 °C), the freezing point of pure water (0.0 °C) and the critical point of water (374.1 °C) were performed. A heating rate of 0.1–0.2 °C/min was adopted near the phase transformation. The precision of measurement was ±0.2 °C at the freezing temperature and ± 2 °C at the homogenization temperature. Salinities (wt% $NaCl_{eqv.}$) and mole fractions of H_2O, $NaCl$ and CO_2 in fluid inclusions were calculated using the Excel program from Steele-MacInnis (2018).

3.5. LA–ICP–MS analysis of quartz and fluid inclusions

Major and trace elements in quartz and fluid inclusions were measured using an Agilent 7900 ICP-MS equipped with a GeoLasPro 193 nm ArF excimer laser. A laser repetition of 10 Hz and an energy density of 10 J/cm^2 were used during the analyses. A laser spot size of 44 μm was used for quartz but was adjusted from 24 to 44 μm for fluid inclusions according to their sizes.

For quartz elemental calibrations, the external standard of NIST SRM610 was used and analyzed twice every 10 analyses. An internal standard–independent calibration strategy, which is based on the normalization of the sum of all metal oxides to 100 wt%, was applied to the quantitative calibrations using the *ICPMSDataCal* software (Liu et al., 2008). NIST SRM612 and NIST SRM614 were analyzed to monitor the accuracy of the results, which show that the uncertainties of the detected elements are mostly better than 10%. A natural quartz standard having well-constrained concentrations for Li, Al and Ti (Audétat et al., 2015) was also analyzed to monitor the accuracy. The analytical results herein are consistent with the recommended values within errors.

For fluid inclusion major and trace elemental calibrations, the raw LA–ICP–MS data were processed using the *SILLS* software (Guillong et al., 2008). NIST SRM610 was used as an external standard and analyzed twice every 10 analyses. The NaCl equivalent wt% concentrations in fluid inclusions obtained independently from microthermometry were used as the internal standard (Heinrich et al., 2003). The charge–balance method was adopted to correct the modelled amounts of Na (from the $NaCl_{eqv.}$ wt%) for salinity contributions of other chloride salts (Allan et al., 2005). Synthetic fluid inclusions containing five elements (Na, K, Ca, Rb and Cs) were analyzed to monitor the accuracy, which show uncertainties less than 16%. More details are described in Lan et al. (2017) and Mu et al. (2021).

3.6. SIMS analysis of quartz

In situ oxygen isotopic compositions ($\delta^{18}O_{VSMOW}$) of quartz were measured using a CAMECA IMS 1280 SIMS at the Institute of Geology and Geophysics, Chinese Academy of Sciences, Beijing, China. The quartz samples were mounted in 25-mm diameter epoxy discs with quartz standards of NBS-28 and Qinghu. The samples were carefully polished and coated with gold before testing. A primary Cs$^+$ ion beam with diameter of ~10 × 15 μm^2 was used. The instrumental mass fractionation factor was corrected using the NBS-28 quartz. The Qinghu quartz was used as a monitoring standard, which shows uncertainties of $\delta^{18}O$ better than 0.3‰ (2SD). More details are described in Tang et al. (2020).

4. Results

4.1. Cathodoluminescence and microtextures of quartz

Quartz grains from different mineralization styles and hydrothermal stages have distinct microtextures. In the Linglong-type mineralization

(Linglong gold deposit), the quartz of hydrothermal stage I (Q1) is commonly coarse-grained and subhedral to anhedral with a homogeneous texture or minor zoning (Figs. 6a and 7a). The stage II quartz (Q2) is coarse- to fine-grained and euhedral to anhedral (Fig. 6b and c), which is typically characterized by oscillatory zoning (Fig. 7b). The stage III quartz (Q3) shows similar features as the Q2, but is coexisting with polymetallic sulfides (Figs. 6d and 7c). The stage IV quartz (Q4) is fine-grained and subhedral to anhedral (Fig. 6e). It is darker than the early-stage quartz under CL imaging with no or weak oscillatory zoning (Fig. 7d and e).

The stage II quartz (Q2) from the Jiaojia-type mineralization (Xiadian and Jiangjiayao gold deposits) is medium- to fine-grained and subhedral to anhedral (Fig. 6f and g). It does not have oscillatory zoning and typically contains tiny silicate (mainly sericite) inclusions (Fig. 7f and g). There is no significant difference between the quartz of the Xiadian and Jiangjiayao deposits.

The igneous and metamorphic quartz grains from the wallrocks are coarse- to medium-grained with subhedral to anhedral shapes (Fig. 6h and i). Both have no zoning. The igneous quartz grains show homogeneous texture, while the metamorphic quartz grains are often deformed and fractured (Fig. 7h and i).

### 4.2. Elemental and isotopic compositions of quartz

A total of ~500 LA–ICP–MS spots were measured for quartz, and ~10% of these analyses were discarded owing to the contamination by mineral and/or fluid inclusions, as displayed in the LA–ICP–MS signals. Lithium, B, Al, Ge and Sb concentrations are much higher in the Linglong-type than in the Jiaojia-type mineralization, but Na, Sr and Ba show opposite trends (Fig. 8; ESM Table S1). Lithium, Al, Ti and Ge are well correlated with each other in the Linglong-type mineralization (Fig. 8a–c), while K, Al and Rb are well correlated in the Jiaojia-type mineralization (Fig. 8d and e). From the early to late hydrothermal stages, the Li and Al concentrations decrease continuously in the Linglong gold deposit (Figs. 8a and 9a). From the deep to shallow depths in the Jiangjiayao and Xiadian deposits, the Sr, Cu, Zn and Pb concentrations decrease with decreasing depth (Fig. 8f–i). The igneous and metamorphic quartz grains have higher Ti but lower Ge concentrations than the hydrothermal quartz (Fig. 8b and c).

The $\delta^{18}O_{VSMOW}$ values of quartz are systematically higher in the Linglong-type than in the Jiaojia-type mineralization (Fig. 9b). The $\delta^{18}O_{quartz}$ values of Q1, Q2, Q3 and Q4 from the Linglong gold deposit are 14.3–16.2‰, 13.2–15.5‰, 13.2–15.2‰ and 13.3–14.9‰, respectively, while those of the Q2 from the Jiangjiayao and Xiadian deposits are 9.7–11.4‰ and 10.7–12.8‰, respectively (Table 2; ESM Table S2). The igneous and metamorphic quartz grains have $\delta^{18}O_{quartz}$ values of 10.7–12.4‰ and 8.4–9.1‰, respectively (Table 2).

4.3. Petrography and Raman spectroscopy of fluid inclusions

Combined with detailed petrographic observations and Raman spectroscopic analyses, three major types and five subtypes of fluid inclusions were identified in Q1 to Q4 from the Linglong gold deposit at ambient temperature (~25 °C):

(1) H_2O–$NaCl$–CO_2 fluid inclusions (HC-type). These fluid inclusions occur in all the hydrothermal stages and are dominant in the Q1 to Q3 (>70% in number), which show liquid H_2O and vapor/liquid CO_2 phases (Figs. 10a–l and 11). They occur isolated or in clusters with sizes of 8–16 μm. According to the volumes of the CO_2 phases (vapor and liquid CO_2), they can be divided into three subtypes: (a) HC$_V$-type, having a large volume of liquid H_2O (>60 vol%) and a small volume of vapor CO_2 (<40 vol%); (b) HC$_{V+L}$-type, having a small volume of liquid H_2O and a large volume of CO_2 phase (commonly >60 vol%), including both the liquid and vapor CO_2 ('double bubbles'); (c) HC$_L$-type, having a
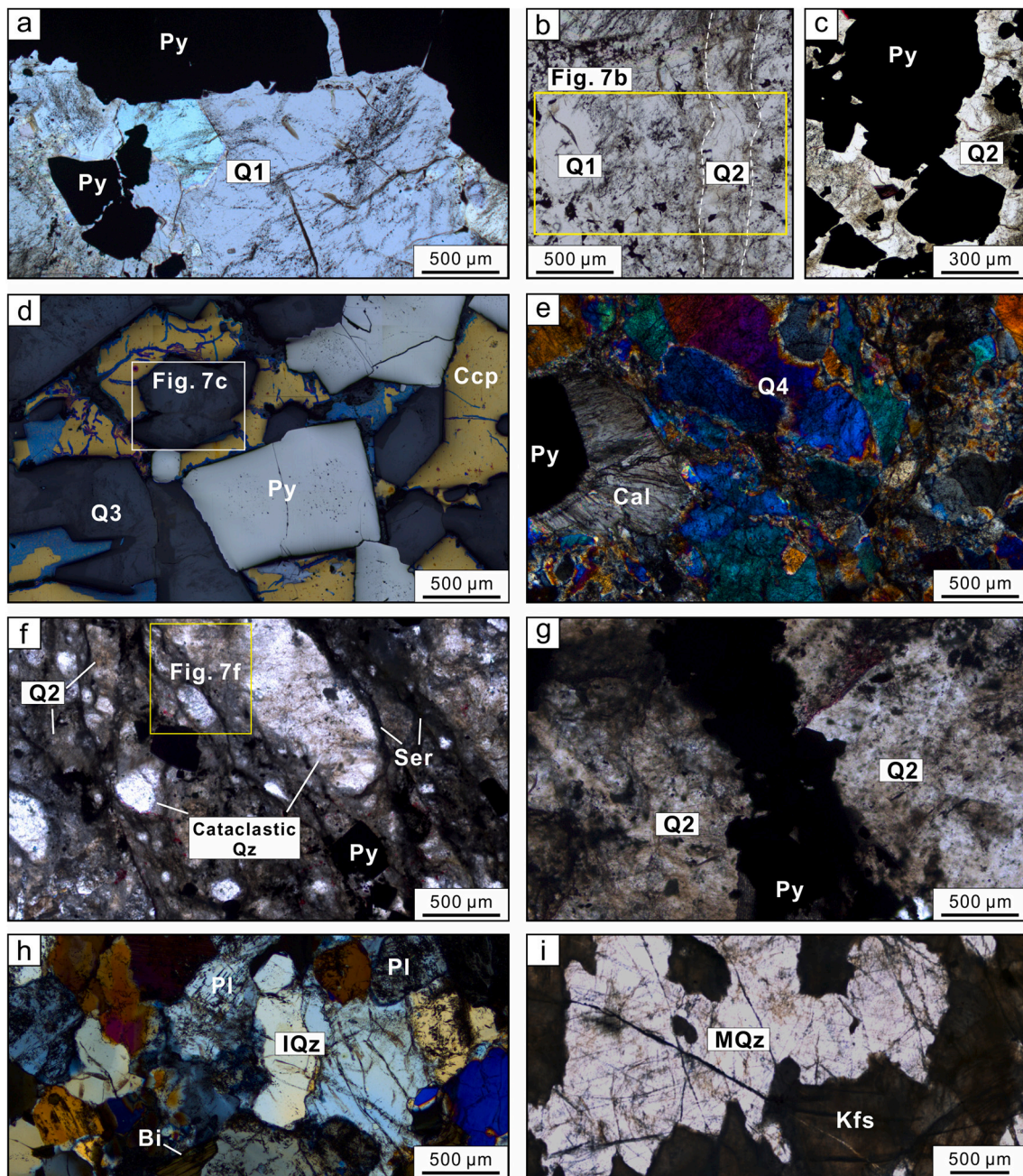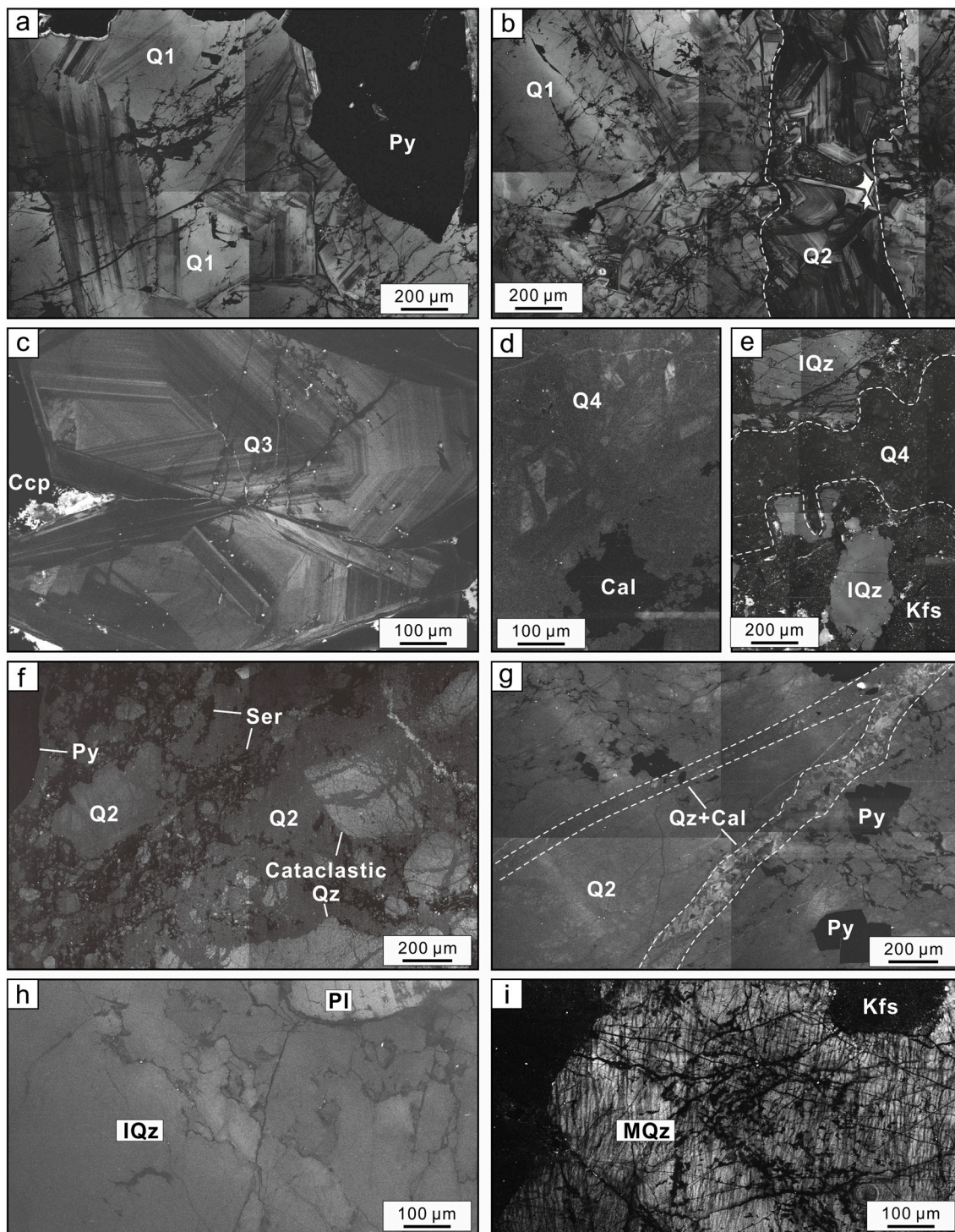
Fig. 6. Microphotographs of hydrothermal, igneous and metamorphic quartz from the Linglong, Xiadian and Jiangjiayao gold deposits. (a–e) Quartz of hydrothermal stage I, II, III and IV from the Linglong gold deposit. (f) Quartz of hydrothermal stage II in disseminated mineralization from the Xiadian gold deposit. (g) Quartz of hydrothermal stage II in stockwork mineralization from the Jiangjiayao gold deposit. (h) Igneous quartz from the Late Jurassic granite. (i) Metamorphic quartz from quartz–K-feldspar pegmatitic vein within the Late Archean gneiss. (d) is under reflected light, (e) and (h) are under crossed polarized light and the others are under plane polarized light. Abbreviations: Py = pyrite; Ccp = chalcopyrite; Q = quartz; Cal = calcite; Ser = sericite; IQz = igneous quartz; MQz = metamorphic quartz; Bi = biotite; Pl = plagioclase; Kfs = K-feldspar. (For interpretation of the references to colour in this figure legend, the reader is referred to the web version of this article.)

small volume of liquid H_2O and a very large volume of liquid CO_2 (commonly >80 vol%). The HC_L-type fluid inclusions mainly occur in Q2 and Q3, but have not been found in Q4. From $HC_V \rightarrow HC_{V+L} \rightarrow HC_L$ fluid inclusions, the CO_2 peaks of Raman spectra show increasing intensities, which are coupled with the CO_2 Fermi diad bands shifting to lower wavenumbers (Fig. 11). These trends indicate the increasing densities of the CO_2 phase and the transformation of vapor CO_2 into liquid CO_2 (Wang et al., 2011). The HC_V-, HC_{V+L}- and HC_L-type fluid inclusions can coexist, but the former two are more common (Fig. 10e–l).

(2) Pure CO_2 fluid inclusions (C-type). These fluid inclusions show vapor CO_2 and liquid CO_2 phases. They occur isolated or in clusters and are commonly oval with sizes smaller than 15 μm. They are less common, but can be found in coexistence with HC-type fluid inclusions (Fig. 10l), especially in Q2 and Q3.

(3) H_2O–NaCl fluid inclusions (H-type). These fluid inclusions have liquid H_2O and vapor H_2O phases. They commonly occur in clusters with polygonal or irregular shapes (Fig. 10m–o). They are widely developed in Q4 as primary inclusions, but occur as secondary inclusions in Q1, Q2 and Q3.

Fig. 7. SEM-CL images of hydrothermal, igneous and metamorphic quartz from the Linglong, Xiadian and Jiangjiayao gold deposits. (a–e) Quartz grains of hydrothermal stage I, II, III and IV from the Linglong gold deposit. (f) Quartz of hydrothermal stage II from the Xiadian gold deposit. (g) Quartz of hydrothermal stage II from the Jiangjiayao gold deposit. (h) Igneous quartz from the Late Jurassic granite. (i) Metamorphic quartz from quartz–K-feldspar pegmatitic vein within the Late Archean gneiss. The abbreviations of minerals are as those in Fig. 6. (For interpretation of the references to colour in this figure legend, the reader is referred to the web version of this article.)

4.4. Microthermometric results of fluid inclusions

During heating, the total homogenization temperatures (Th$_{tot}$) of fluid inclusions in Q1, Q2, Q3 and Q4 are 303 °C–369 °C, 295 °C–345 °C, 289 °C–342 °C and 182 °C–330 °C, respectively (Fig. 12a; ESM Table S3). The HC$_V$-type fluid inclusions were homogenized to a liquid phase, whereas those of the HC$_L$-type were homogenized to a vapor phase. The HC$_{V+L}$-type fluid inclusions can be homogenized to either a liquid or a vapor phase, depending on the CO$_2$ volume. Owing to the large volume of the CO$_2$ bubble in the HC$_L$-type fluid inclusions, the final homogenization can hardly be observed, leading to the higher uncertainties or the failed acquisition of the Th$_{tot}$. Specifically, the Th$_{tot}$ of the HC$_V$- and HC$_{V+L}$-type fluid inclusions in Q1 is 303 °C–369 °C and 312 °C–364 °C, respectively. The Th$_{tot}$ of the HC$_V$-, HC$_{V+L}$- and HC$_L$-type
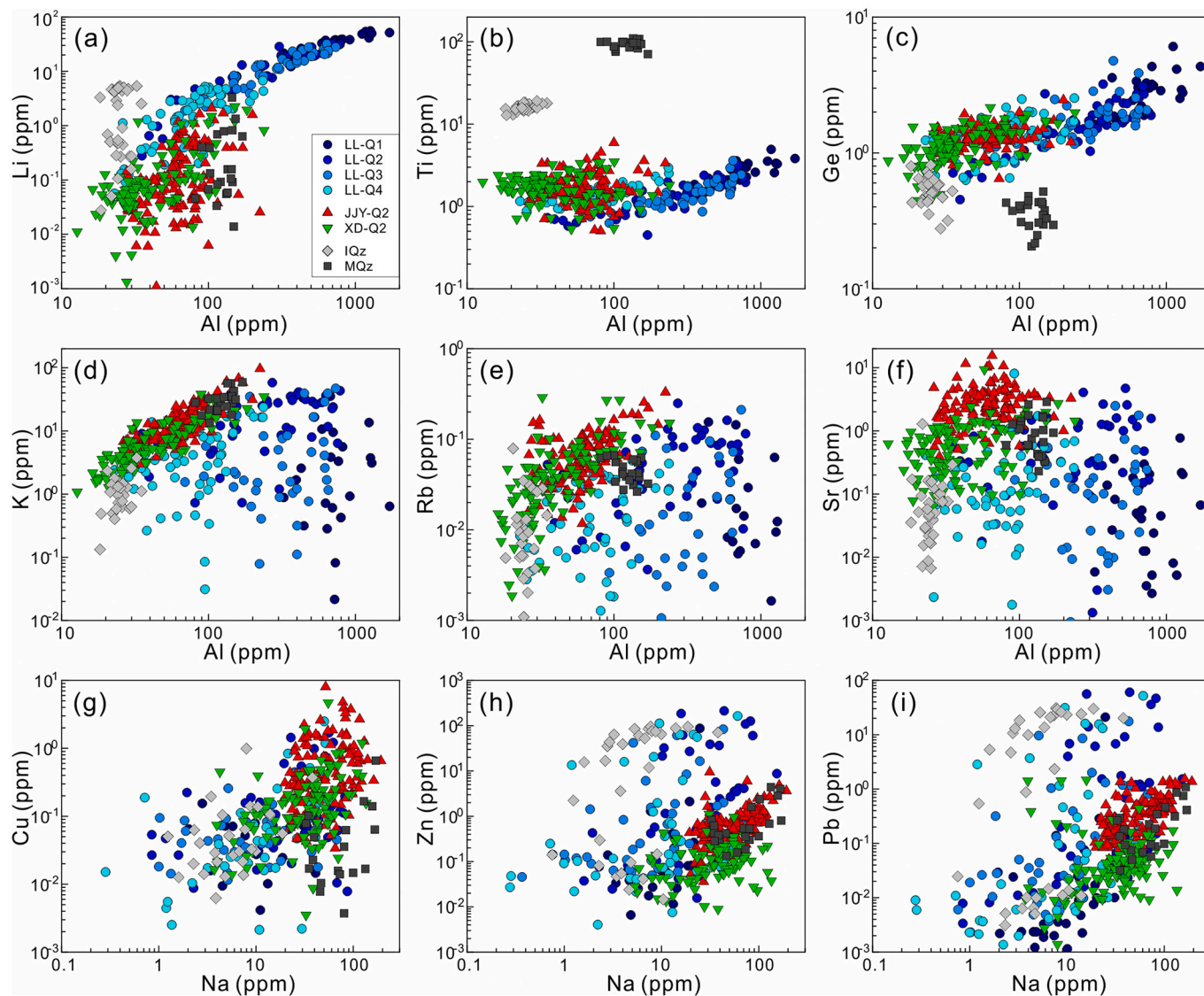
Fig. 8. Binary plots of elemental concentrations in quartz from the Linglong, Xiadian and Jiangjiayao gold deposits. Abbreviations: LL = Linglong gold deposit; JJY = Jiangjiayao gold deposit; XD = Xiadian gold deposit; Q = quartz; IQz = igneous quartz; MQz = metamorphic quartz. (For interpretation of the references to colour in this figure legend, the reader is referred to the web version of this article.)
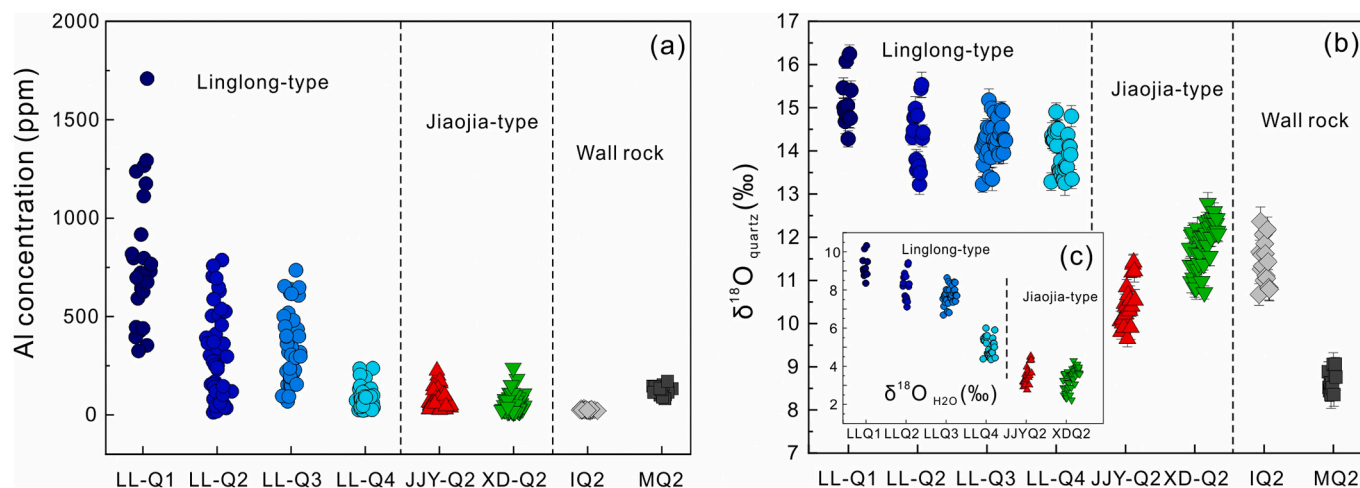
Fig. 9. Variations of Al concentrations (a), $\delta^{18}O_{quartz}$ (b) and equilibrated $\delta^{18}O_{H2O}$ (c) in quartz from the Linglong, Xiadian and Jiangjiayao gold deposits. (For interpretation of the references to colour in this figure legend, the reader is referred to the web version of this article.)

Table 2

Summary of SIMS oxygen isotopic compositions of quartz and the equilibrated fluids from the Linglong, Xiadian and Jiangjiayao gold deposits.

Location	Sample	Hydrothermal stage	$\delta^{18}O_{quartz}$ (‰)	T (°C)	$\delta^{18}O_{H2O}$ (‰)
Linglong deposit	17LL07–1A	Stage I	14.3–16.2	329	8.4–10.3
	17LL07	Stage II	13.2–15.5	323	7.1–9.4
	17LL13B	Stage III	13.2–15.2	310	6.7–8.6
	17LL15B	Stage IV	13.3–14.9	251	4.4–6.0
	17LL23A	Stage IV	13.3–14.8	251	4.4–5.9
	17LL23B	IQz	10.7–12.4		
Xiadian deposit	17XD11B	Stage II	10.7–12.2	260	2.2–3.7
	17XD12	Stage II	11.6–12.8	260	3.1–4.3
	17XD01	MQz	8.4–9.1		
Jiangjiayao deposit	17JJY07	Stage II	9.7–10.9	300	2.8–4.0
	17JJY24–1	Stage II	9.9–11.4	300	3.0–4.5

Notes: The temperatures (T/°C) used for calibrating the $\delta^{18}O_{H2O}$ of the equilibrated fluids in Q1, Q2 and Q3 from the Linglong gold deposit are the mean Th_{tot} of the HC_V-type fluid inclusions, based on the suggestion of Diamond (2001) that the Th_{tot} of the endmember fluid inclusions (either the aqueous liquid or the carbonic liquid endmember) are closer to the entrapment temperature. In Q4, due to the fluid mixing (e.g., occurrence of primary H-type fluid inclusions), the mean Th_{tot} of the HC_V- and H-type fluid inclusions is adopted. Those for the Xiadian and Jiangjiayao gold deposits are referred to Chai et al. (2017) and Liu et al. (2018). Abbreviations: IQz = igneous quartz; MQz = metamorphic quartz.

fluid inclusions in Q2 is 310 °C–338 °C, 295 °C–345 °C and 327 °C–329 °C, respectively. In Q3, the HC_V-, HC_{V+L}- and HC_L-type fluid inclusions have a Th_{tot} of 287 °C–334 °C, 290 °C–340 °C and 290 °C–342 °C, respectively. The Th_{tot} decreases significantly in Q4, showing 267 °C–282 °C, 254 °C–330 °C and 182 °C–277 °C for the HC_V-, HC_{V+L}- and H-type fluid inclusions, respectively.

During cooling, the HC-type fluid inclusions were completely frozen at temperatures between −90 °C and − 100 °C, while the H-type fluid inclusions were frozen at temperatures between −30 °C and − 40 °C. Melting of solid CO_2 occurred at temperatures between −58.1 °C and − 56.6 °C (Tm_{CO2}), which are equal to or slightly lower than the triple-point temperature of pure CO_2 (−56.6 °C). This indicates that CO_2 is the dominant volatile species in the fluid inclusions, but minor other species such as CH_4 might also be present, as indicated by Raman spectroscopy (Wen et al., 2015). The CO_2 clathrates melted at temperatures (Tm_{clath}) between 4.5 °C and 9.6 °C. Specifically, the Tm_{clath} of the HC_V- and HC_{V+L}-type fluid inclusions in Q1 is 4.7 °C–8.7 °C and 4.5 °C–8.7 °C, respectively. In Q2, the Tm_{clath} of the HC_V-, HC_{V+L}- and HC_L-type fluid inclusions is 6.2 °C–8.7 °C, 6.8 °C–8.8 °C and 7.4 °C–8.4 °C, respectively. The HC_V-, HC_{V+L}- and HC_L-type fluid inclusions in Q3 show a Tm_{clath} of 6.5 °C–8.2 °C, 6.8 °C–9.6 °C and 7.1 °C–8.7 °C, respectively. In Q4, the Tm_{clath} of the HC_V-type and HC_{V+L}-type fluid inclusions is 6.8 °C–8.1 °C and 5.8 °C–8.5 °C, respectively. Based on the Tm_{clath}, using the equations of Bakker et al. (1996), the corresponding salinities of the HC-type fluid inclusions in Q1, Q2, Q3 and Q4 are 2.6–9.8 wt% $NaCl_{eqv}$, 2.4–7.1 wt% $NaCl_{eqv}$, 0.8–6.6 wt% $NaCl_{eqv}$ and 3.0–7.8 wt% $NaCl_{eqv}$, respectively (Fig. 12b; ESM Table S3). For the primary H-type fluid inclusions in Q4, the ice melting temperatures (Tm_{ice}) vary from −5.0 °C to −1.3 °C, corresponding to the salinities of 2.2–7.9 wt% $NaCl_{eqv}$.

Partial homogenization of the CO_2 phases for the HC-type fluid inclusions occurred at temperatures between 15.5 °C and 31.1 °C (Th_{CO2}). The CO_2 phases (liquid and vapor CO_2) were homogenized to the vapor phase in HC_V-type fluid inclusions, but to the liquid phase in the HC_L-type fluid inclusions. For the HC_{V+L}-type fluid inclusions, partial homogenization of CO_2 can occur either to the vapor or the liquid phase, but mostly to the vapor phase. In Q1, the Th_{CO2} of the HC_V- and HC_{V+L}-type fluid inclusions is 15.5 °C–23.7 °C and 23.4 °C–31.1 °C, respectively. In Q2, the Th_{CO2} of the HC_V-, HC_{V+L}- and HC_L-type fluid inclusions is 23.0 °C–25.1 °C, 25.9 °C–31.1 °C and 20.1 °C–25.1 °C, respectively. In Q3, the HC_V-, HC_{V+L}- and HC_L-type fluid inclusions show

a Th_{CO2} of 22.1 °C–24.8 °C, 25.3 °C–31.1 °C and 22.8 °C–24.0 °C, respectively. In Q4, the Th_{CO2} of the HC_V- and HC_{V+L}-type fluid inclusions is 23.3 °C–23.6 °C and 26.0 °C–31.1 °C, respectively. Based on the measured Tm_{clath}, Th_{CO2} and Th_{tot} (or the volume fractions of the homogenized CO_2 phase), the mole fractions of CO_2 (X_{CO2}) can be estimated using the Excel program from Steele-MacInnis (2018). Consequently, the X_{CO2} of the HC-type fluid inclusions in Q1, Q2, Q3 and Q4 is estimated to be 0.06–0.11, 0.07–0.75, 0.06–0.43 and 0.05–0.26, respectively (ESM Table S3). The C-type fluid inclusions were commonly homogenized to the vapor phase at temperatures of 27.2 °C–31.1 °C.

4.5. Major and trace elements of fluid inclusions

Because the C- and H-type fluid inclusions are rare or secondary, just the primary HC-type fluid inclusions were subject to LA–ICP–MS analysis (Fig. 13). Sodium and K are the most abundant elements, with concentrations of 4000–29,000 ppm and 270–14,000 ppm, respectively (Table 3; ESM Table S4). The K/Na mass ratios vary from 0.02 to 1.66, with the majority ranging between 0.1 and 1.0. Strontium, Ba, Pb and Rb are less abundant, showing concentrations of 20–300 ppm, 10–200 ppm, 2–200 ppm and 1–50 ppm, respectively. Other elements such as Mn, Fe, Zn, Cu, As and Sb can be sporadically detected. Gold was not detected, and just several inclusions have Ag concentrations higher than the detection limit. The HC-type fluid inclusions from different hydrothermal stages do not show significant difference in elemental compositions (Table 3; ESM Table S4).

5. Discussion

5.1. Temporal evolution of the ore-forming fluids and gold deposition

Multiple stages of hydrothermal fluids occurred in the Jiaodong gold deposit, of which the Au was dominantly deposited at the quartz–pyrite and quartz–polymetallic sulfide stages. This implies that some unusual processes might contribute to the focused Au deposition. Gold deposition can be induced by the changes in temperature, pressure, acidity, salinity, oxygen and sulfur fugacities of the fluids, which are commonly associated with geological processes such as fluid cooling, mixing/unmixing and fluid–rock interaction (Williams-Jones et al., 2009; Pokrovski et al., 2014). The Th_{tot} values of fluid inclusions in the Linglong deposit decrease slightly from Q1 to Q3 but significantly to Q4 (Fig. 12a). The $\delta^{18}O_{H2O}$ values of the fluids equilibrated with Q1, Q2, Q3 and Q4 are calculated to be 8.4–10.3‰, 7.1–9.4‰, 6.7–8.6‰ and 4.4–6.0‰ (Table 2), respectively, also showing a decrease to Q4 (Fig. 9c). The coupled decrease of Th_{tot} and $\delta^{18}O_{H2O}$ values, combined with the development of H-type fluid inclusions in Q4, suggest that fluid mixing with meteoric water likely occurred in the final hydrothermal stage (Wen et al., 2015), but not during the pre-mineralization and ore-forming stages. Fluid cooling or mixing could not be responsible for the massive Au deposition. The mineral assemblages of different hydrothermal stages (stage I to III) in the Linglong gold deposit as well as in the other Jiaodong gold deposits are mainly composed of quartz + sulfide without magnetite/hematite or sulfate (Figs. 4 and 5), implying that oxygen fugacity changed little throughout the hydrothermal evolution. In addition, considering the distinct contacts between the ore veins and the wallrocks in the Linglong gold deposit (Fig. 4a), gold deposition could not be induced by fluid–rock interaction, at least not in the Linglong-type mineralization.

Different types of fluid inclusions (e.g., HC_V-, HC_{V+L}-, HC_L- and C-type) are commonly coexisting in Q2 and Q3 from the Linglong gold deposit (Figs. 10 and 11). In addition, the HC_V-, HC_{V+L}- and HC_L-type fluid inclusions have similar Th_{tot} (Fig. 12a). Considering that fluid–fluid unmixing of H_2O–CO_2–NaCl system often results in the coexistence of CO_2-rich (e.g., the HC_L- and C-type fluid inclusions) and H_2O-rich (e.g., the HC_V-type fluid inclusions) fluid endmembers with variable intermediate phases (e.g., the HC_{V+L}-type fluid inclusions) (Ramboz et al.,
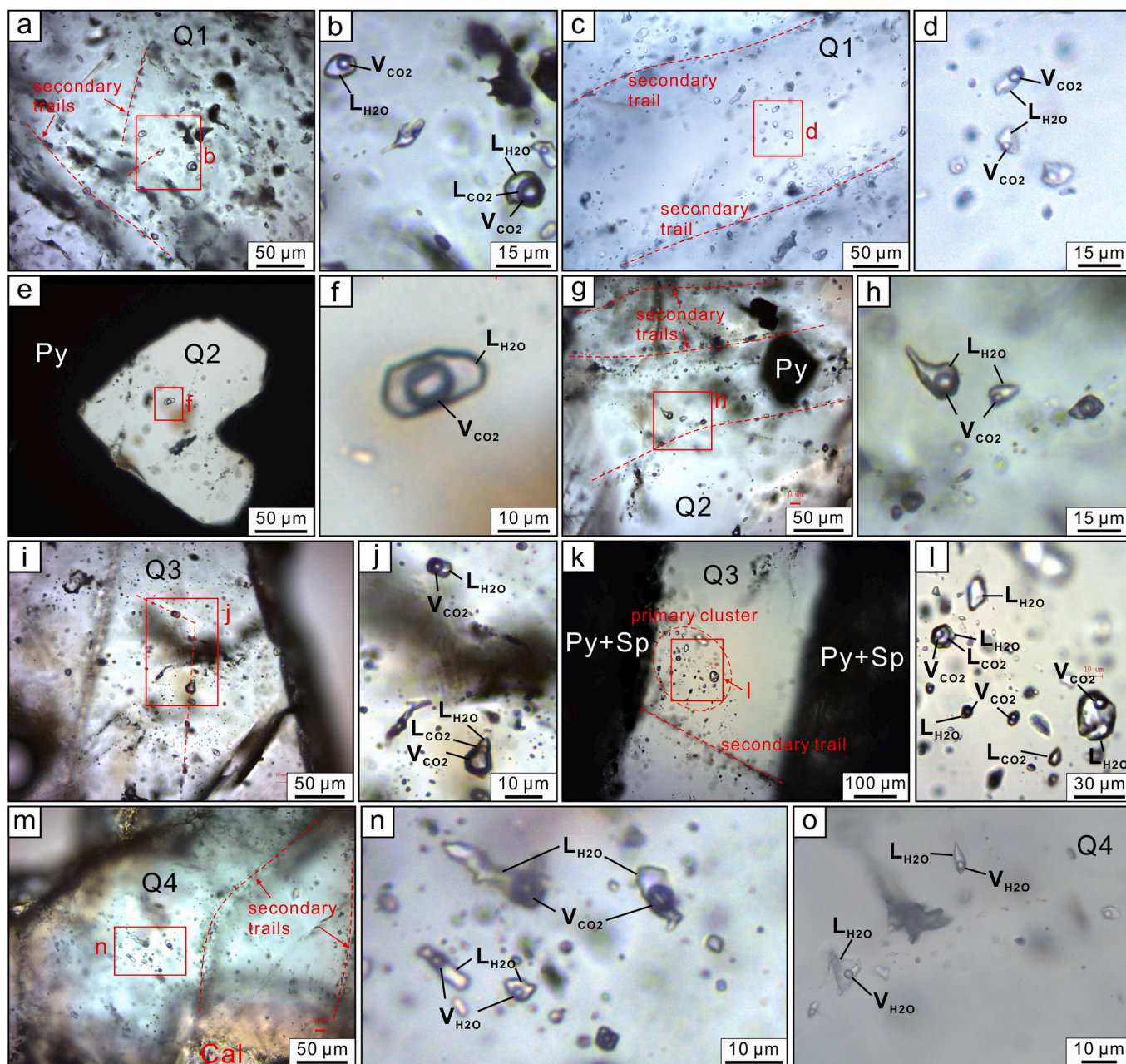
Fig. 10. Fluid inclusions in different stages of quartz from the Linglong gold deposit. (a–d) HC-type fluid inclusions in Q1. (e–l) HC-type fluid inclusions in Q2 and Q3, showing the coexistence of vapor-rich and liquid-rich inclusions. (m–o) Primary and secondary H-type fluid inclusions in Q4. Abbreviations: L = liquid, V = vapor. (For interpretation of the references to colour in this figure legend, the reader is referred to the web version of this article.)

1982; Diamond, 2001), the above phenomena strongly indicate fluid-–fluid unmixing in the ore-forming stages. In addition, the Q2 and Q3 grains from the Linglong deposit typically show oscillatory zoning under CL imaging (Fig. 7b and c). Oscillatory zoning commonly reflects fine-scale chemical variations caused by changes in fluid composition, pressure, temperature and mineral growth rate (Barker and Cox, 2011; Götte et al., 2011), which can be easily induced by fluid unmixing (e.g. Müller et al., 2010; Maydagán et al., 2015). Actually, fluid unmixing has been widely observed in the gold deposits from the Jiaodong Peninsula (e.g. Fan et al., 2007; Wen et al., 2015, 2016; Guo et al., 2017; Liu et al., 2018), indicating that it was a common process occurring in these deposits. Fluid unmixing can lead to the release of CO_2 into the vapor phase (CO_2 degassing) and increase the pH of the liquid phase (Drummond and Ohmoto, 1985; Phillips and Evans, 2004; Kokh et al., 2017). Based on the PTX-pH properties of the H_2O–CO_2–NaCl system (Li and

Duan, 2007; Truche et al., 2016), combined with the microthermometric data (e.g., Tm_{clath} and Th_{tot}), the pH values of the captured fluids in the studied deposit are estimated to be 3–5. Fluid unmixing could have elevated the pH by 1–2 units owing to the loss of CO_2. In the reduced H–O–S–Cl hydrothermal fluids with low salinities (e.g. 1–2 m NaCl) and moderate to low temperatures (e.g. 200 °C–400 °C), the solubilities of Au and Ag as well as those of Cu, Zn and Pb decrease sharply from acidic (e.g. pH < 3) to neutral conditions (e.g. pH of 4–6) (Reed and Palandri, 2006; Pokrovski et al., 2013, 2014). Consequently, a slight increase of pH would cause metal precipitation. Aluminium concentrations in hydrothermal quartz are highly associated with pH, which will increase significantly as the pH decreases (Rusk et al., 2008). The Al concentrations show a continuous decrease from Q1 to Q4 in the Linglong gold deposit (Figs. 8a and 9a), which is consistent with a pH increase. In conclusion, the physic-chemical conditions of the ore-forming fluids
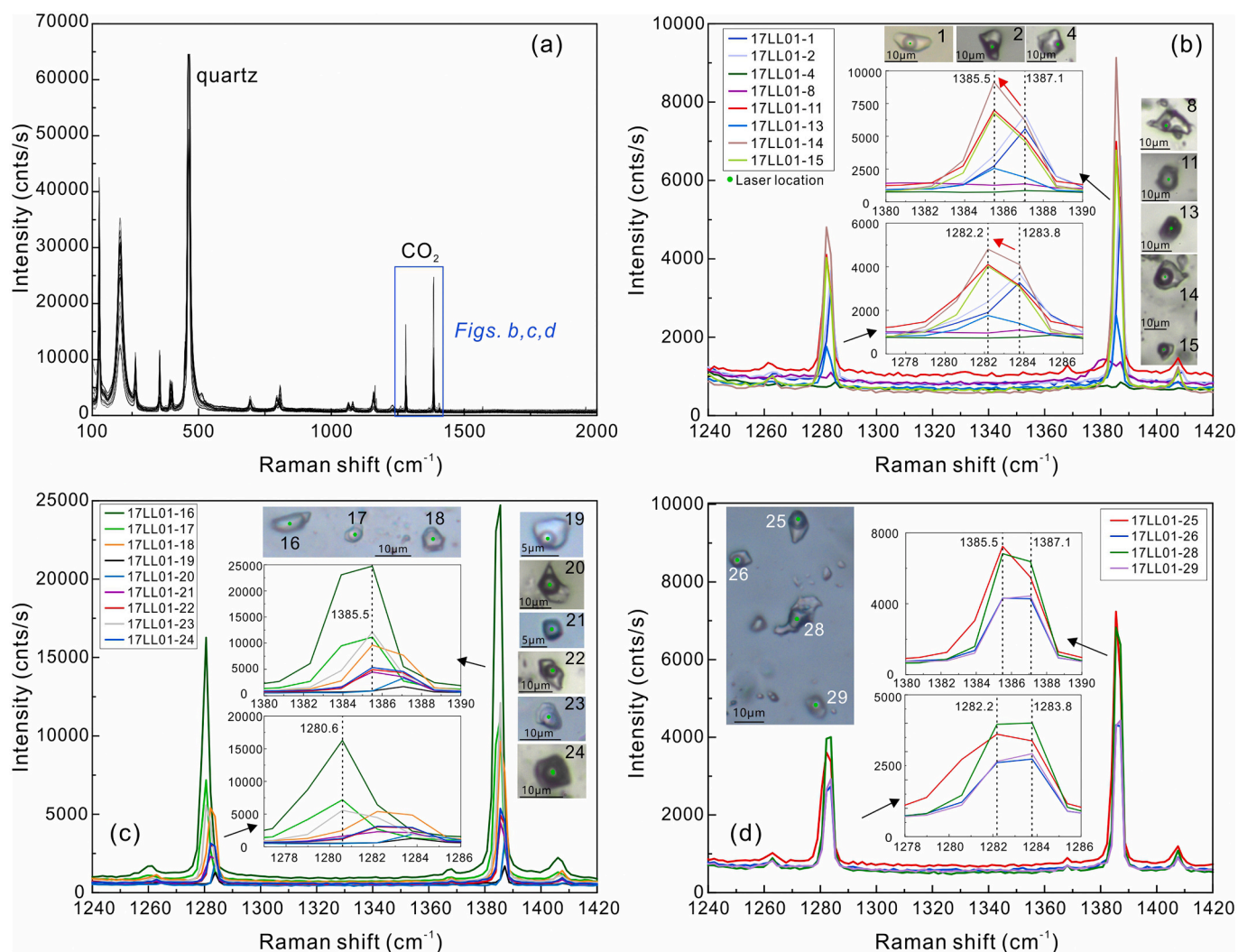
Fig. 11. Representative Raman spectra of CO_2-bearing fluid inclusions in quartz (a), and the changeable intensities of CO_2 peaks and Fermi diad bands for different fractions of CO_2 (b–d). Note that the higher fractions of CO_2 the stronger intensities of the CO_2 peaks. The CO_2 Fermi diad bands shift to lower wavenumbers from the vapor CO_2 (e.g., 1387–1388 cm^{-1} and 1282–1285 cm^{-1}) to the liquid CO_2 (e.g., 1382–1385 cm^{-1} and 1281–1282 cm^{-1}) (Wang et al., 2011).

changed over time, especially the pH increased owing to the CO_2 degassing during fluid–fluid unmixing. This could have led to the Au precipitation during a relatively short time interval.

5.2. Spatial variations of the ore-forming fluids

Previous studies showed that the Th_{tot} and salinities of fluid inclusions from the ore-forming stages of the Jiaodong gold deposits do not change too much within the depth range of 0 to −4000 m (Wen et al., 2016; Liu et al., 2018). This implies that the fluid properties (e.g. salinity and temperature) might remain stable during upward transport. However, the in situ geochemistry of quartz indicates that some vertical changes occurred. For example, the Cu, Pb and Zn concentrations in Q2 decrease from the Jiangjiayao to the Xiadian samples, while the $\delta^{18}O_{quartz}$ values increase (Figs. 8g–i and 9b). Because Cu, Pb and Zn can hardly enter the structure of quartz due to their distinct ionic radius to Si, their occurrences in quartz are mainly associated with fluid/mineral inclusions (Götze et al., 2004). The higher Cu, Pb and Zn concentrations in the deeper quartz imply that the original ore-forming fluids were richer in these metals. Combined with polymetallic sulfides rarely occurring in deep depths but being abundant in shallow depths, it is inferred that these metals were gradually fractionated from the fluids during upward transport owing to the deposition of polymetallic

sulfides.

The $\delta^{18}O_{quartz}$ values of Q2 increase slightly from 9.7–11.4‰ to 10.7–12.8‰ from the Jiangjiayao to the Xiadian samples, and are significantly higher (13.2–15.5‰) in the Linglong samples (Fig. 9b). The increase in $\delta^{18}O_{quartz}$ can be potentially induced by fluid–rock interaction or by isotopic fractionation during cooling (Taylor, 1974; Zhang et al., 1989). The Th_{tot} values of fluid inclusions from the ore-forming stages (stages II and III) do not show a significant decrease from −1445 m to −517 m in the Xiadian deposit (Liu et al., 2018), implying that cooling contributed little to the increase of $\delta^{18}O_{quartz}$. Actually, the Th_{tot} values are 180 °C–300 °C (peak of 240 °C–260 °C for stages II and III) in the Xiadian deposit (Chai et al., 2017; Liu et al., 2018), which are lower than those of the Linglong deposit (peak of 310 °C–330 °C; Fig. 12a). The deeper samples have lower Th_{tot} and $\delta^{18}O_{quartz}$ values, clearly indicating that cooling was not responsible for the increase of $\delta^{18}O_{quartz}$. In addition, if using the peak Th_{tot} (260 °C) for calibration, the $\delta^{18}O_{H2O}$ values of the ore-forming fluids for the Xiadian deposit would be 2.2–4.3‰, which are remarkably lower than those of the Linglong deposit (6.7–9.4‰ for stages II and III; Fig. 9c; Table 2) and also much lower than many other Jiaodong gold deposits (commonly >5‰) (Mao et al., 2008). The $\delta^{18}O_{H2O}$ values lower than 5‰ in the Jiaodong gold deposits were commonly attributed to the contamination by meteoric water (Mao et al., 2008; Li et al., 2015). Considering the
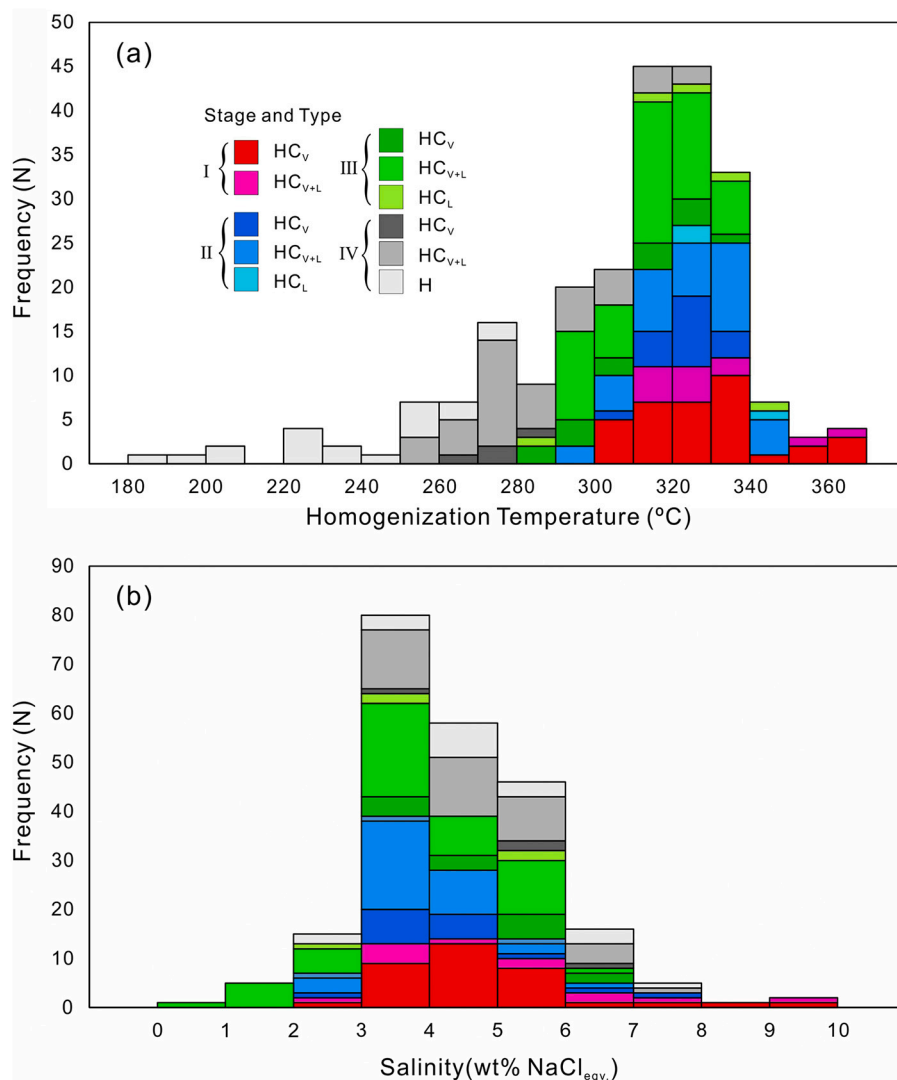
Fig. 12. Histograms showing the homogenization temperatures (a) and salinities (b) of primary fluid inclusions in different stages of quartz from the Linglong gold deposit. (For interpretation of the references to colour in this figure legend, the reader is referred to the web version of this article.)

uniform genesis of these gold deposits (Goldfarb and Santosh, 2014; Deng et al., 2020), it is unlikely that such abnormal low-$\delta^{18}O_{H2O}$ fluids occurred at deep depths.

The lithophile elements such as K, Rb and Al in quartz are well correlated with each other in the Jiangjiayao and Xiadian samples (Fig. 8d and e). In combination with their quartz veinlets dispersed in the altered granites and many sericite inclusions occurring in the quartz grains (Figs. 4f, g and 7f, g), enhanced fluid–rock interaction should have occurred in these deposits. The effects of fluid–rock interaction on the oxygen isotopic compositions of the fluids are modelled for different water/rock ratios (0.001 to 10) and temperatures (from 240 °C to 500 °C) using the method of Taylor (1974). The whole-rock $\delta^{18}O$ value of ~9‰ from the Late Jurassic granites (Mao et al., 2008) and the least contaminated $\delta^{18}O_{H2O}$ value of ~9‰ from the lode-type mineralization in the Linglong deposit (Fig. 9b; Table 2) are used to represent the $\delta^{18}O$ values of the rock and fluid endmembers, respectively. The modelling results show that at temperatures of 240 °C–300 °C, the $\delta^{18}O_{H2O}$ values of the fluids will decrease from ~9‰ to 2.5–4.4‰ as the water/rock ratio decreases from 10 to 0.01, indicating that fluid–rock interaction could significantly lower the $\delta^{18}O_{H2O}$. If the water/rock ratio decreases to 0.01 and 0.1, respectively, the $\delta^{18}O_{H2O}$ values of 2.5–4.4‰ and 3.4–5.1‰ will be obtained (Fig. 14), which generally satisfy the $\delta^{18}O_{H2O}$ variations from the Jiangjiayao to the Xiadian samples. The lower

water/rock ratio at deeper depth suggests that the elevated pressure facilitated fluid dispersion into the wallrocks, which is favorable for fluid–rock interaction. The high water/rock ratio required for the Linglong samples (>3; Fig. 14) supports that wallrocks contributed little to the Linglong-type mineralization.

The above results indicate that the ore-forming fluids were modified during upward migration, especially by fluid–rock interaction, leading to the spatial variations of the elemental and isotopic compositions.

5.3. Contrasted ore-forming processes between the Linglong- and Jiaojia-type mineralization

It is notable that the Linglong- and Jiaojia-type mineralization styles have systematic differences in mineral textures and elemental and isotopic compositions. In the Linglong-type mineralization, the quartz grains are characterized by oscillatory zoning with euhedral to subhedral shapes (Fig. 7b and c), combined with the unmixing features of fluid inclusions (Fig. 10), indicating their precipitation mainly in open fractures (Müller et al., 2010; Maydagán et al., 2015). In the Jiaojia-type mineralization, the quartz grains are characterized by granular mosaics with homogeneous textures (Fig. 7f and g), suggesting their formation mainly under lithostatic conditions (Maydagán et al., 2015; Mao et al., 2017). The above differences could be attributed to the different
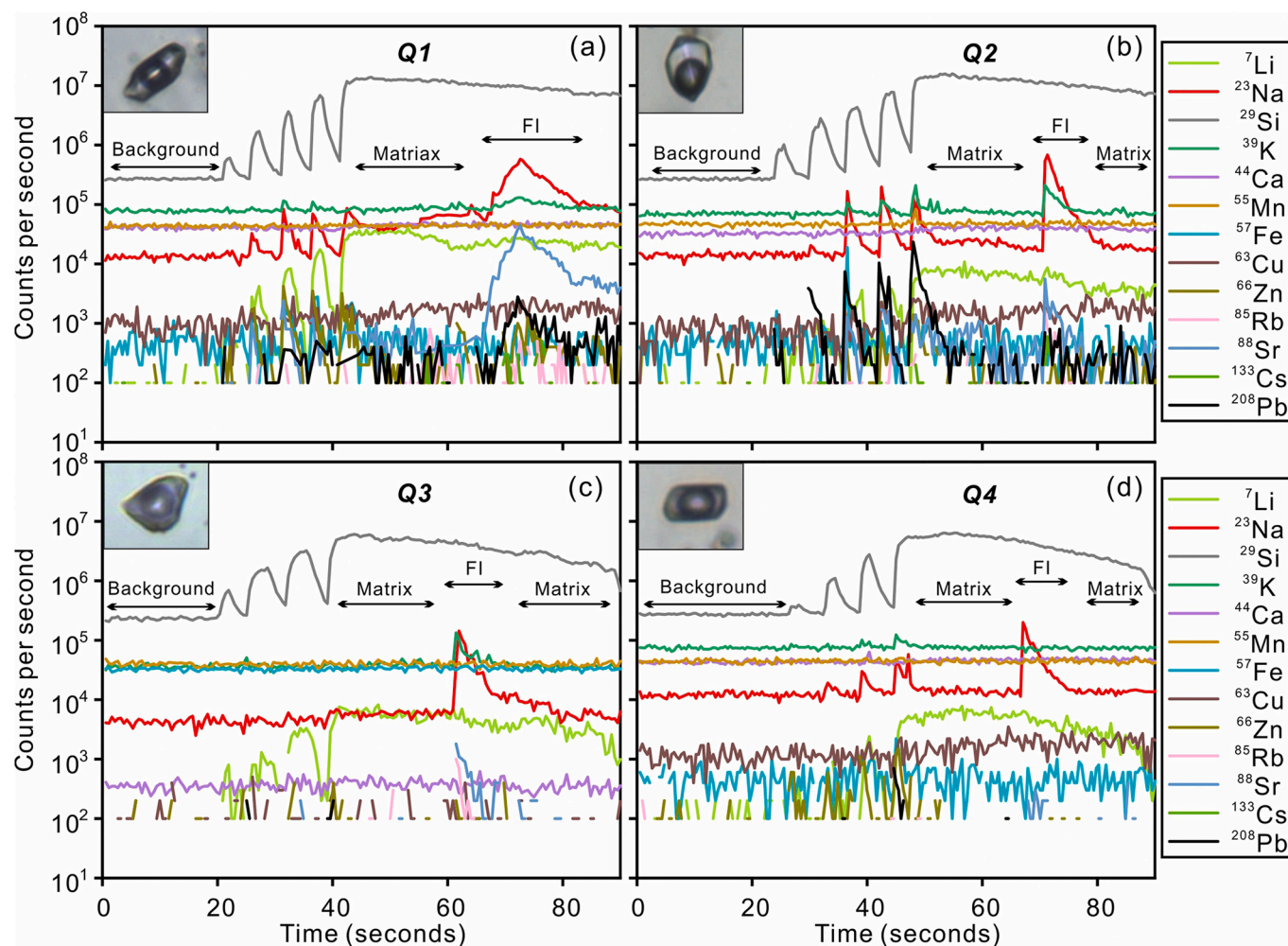
Fig. 13. Representative LA–ICP–MS signals of HC-type fluid inclusions in different stages of quartz (Q1 to Q4) from the Linglong gold deposit. (For interpretation of the references to colour in this figure legend, the reader is referred to the web version of this article.)

structural settings, where the Linglong-type mineralization occurred in the extensional settings, while the Jiaojia-type in the compressional settings (Qiu et al., 2002). The extensional settings facilitated fast fluid migration and unmixing, leading to the formation of quartz lodes. The compressional settings provided limited space for mineral crystallization, but were favorable for fluid–rock interaction, resulting in disseminated and stockwork mineralization.

The distinct ore-forming processes between the Linglong- and Jiaojia-type mineralization are also supported by the elemental and isotopic compositions. The Linglong-type mineralization is characterized by higher Al concentrations and $\delta^{18}O_{quartz}$ values in quartz than the Jiaojia-type mineralization (Figs. 8 and 9). The quartz grains from the Jiaojia-type mineralization show good correlations between lithophile elements (e.g. K, Al and Rb) and have much lower $\delta^{18}O_{quartz}$ values. Because the Al concentrations in quartz are highly associated with pH (Rusk et al., 2008), the ore-forming fluids of the Linglong-type mineralization might be more acidic than those of the Jiaojia-type mineralization. This could be attributed to the high CO_2 contents dissolved in the fluids (Li and Duan, 2007). Because CO_2 is highly incompatible with H_2O, fluid–fluid unmixing can easily occur in the extensional settings due to pressure decrease (Weatherley and Henley, 2013; Cox, 2016). Consequently, an increase in the pH induced by CO_2 degassing typically occurred in the Linglong-type mineralization, leading to the efficient deposition of Au, Ag, Cu, Zn and Pb. For the Jiaojia-type mineralization, the well-correlated lithophile elements and the much lower $\delta^{18}O_{SiO2}$ values in quartz indicate significant fluid–rock interaction, which

increased the pH and thus led to the Au deposition (Li et al., 2013).

5.4. Property and genetic classification of the ore-forming fluids

As introduced before, all kinds of fluids have been proposed as the ore-forming fluids of the Jiaodong gold deposits. Because fluids stemming from different sources can result in different alteration types, mineral assemblages and fluid inclusions, detailed investigations and comparisons with other types of hydrothermal gold deposits were conducted to clarify the properties and genetic type of the auriferous fluids for the studied deposits (Table 4; Figs. 15, 16 and 17).

The hydrothermal alterations in the studied deposits (also for most of the Jiaodong gold deposits) are characterized by K-feldspathization, silicification, sericitization, sulfidation, and minor carbonatization. The mineral assemblages are simple, comprising quartz ± sulfides (mainly pyrite, minor chalcopyrite, pyrrhotite, galena and sphalerite) in the Au-bearing lodes or veinlets. These features are similar to those of the orogenic gold deposits (Table 4). Epithermal gold deposits commonly contain assemblages of quartz + adularia ± illite ± calcite under low-sulfidation conditions or assemblages of quartz + alunite ± pyrophyllite ± dickite ± kaolinite under high-sulfidation conditions (Simmons et al., 2005), both of which are not developed in the studied deposits. The lack of potassic alteration and quartz–sulfide veins in the Carlin-type gold deposits (Cline, 2018) differs from those of the studied deposits. In addition, invisible gold in As-rich pyrite or arsenopyrite is widely developed in the Carlin-type gold deposits (Cline, 2018), but

15

Table 3

Summary of LA–ICP–MS elemental compositions (ppm) of fluid inclusions from the Linglong gold deposit.

Hydrothermal stage	Sample	Value	Salinity	^{7}Li	^{9}Be	^{23}Na	^{39}K	^{55}Mn	^{57}Fe	^{63}Cu	^{66}Zn	^{75}As	^{85}Rb	^{88}Sr	^{107}Ag	^{118}Sn	^{121}Sb	^{133}Cs	^{137}Ba	^{208}Pb
Stage I	17LL07–1A	minimum	3.95	41.3	61.0	10,700	463	75.1	160	13.1	16.2	–	6.30	18.3	–	21.7	16.9	1.47	19.9	6.17
		max	6.12	793	251	20,900	8180	1820	2140	559	1760	–	29.3	541	–	77.2	77.6	4.84	194	1140
		mean	4.73	322	142	16,100	3770	781	971	158	502	–	17.3	133	–	49.4	38.2	2.76	59.6	318
		N	14	5	5	14	13	3	4	4	5	–	11	13	–	2	7	4	7	7
	17LL09B	minimum	4.50	–	–	9240	274	78.9	1690	35.0	47.9	4.89	8.54	56.1	0.29	12.2	3.52	–	13.4	3.56
		max	4.50	–	–	17,400	14,300	1320	3500	35.0	786	4.89	28.7	396	6.05	12.2	43.6	–	244	285
		mean	4.50	–	–	13,900	6270	559	2590	35.0	360	4.89	15.9	193	3.17	12.2	23.6	–	104	104
		N	9	–	–	9	9	6	2	1	6	1	7	9	2	1	2	–	9	9
	17LL09C	minimum	2.62	3.43	167	9450	936	230	–	8.56	194	51.9	6.83	41.2	0.57	28.5	24.0	1.38	10.5	15.3
		max	5.59	139	449	18,000	6860	230	–	8.56	194	54.4	13.8	210	0.57	28.5	30.3	1.38	66.2	15.3
		mean	4.15	72.5	255	14,400	3280	230	–	8.56	194	53.1	10.9	78.2	0.57	28.5	27.2	1.38	43.9	15.3
		N	8	5	6	8	8	1	–	1	1	2	5	8	1	1	2	1	4	1
Stage II	17LL01A	minimum	2.62	26.1	–	7010	481	376	1000	24.8	26.2	18.7	4.92	17.1	46.4	–	15.9	1.26	6.02	3.74
		max	4.32	35.1	–	15,400	5490	376	1690	176	457	18.7	30.1	158	46.4	–	26.5	4.09	32.4	168
		mean	3.41	30.9	–	11,700	2590	376	1350	114	251	18.7	12.7	55.3	46.4	–	20.5	2.47	32.4	45.5
		N	18	3	–	18	16	1	2	6	4	1	13	16	1	–	3	4	6	8
	17LL01B	minimum	3.50	–	–	8730	271	13.0	341	16.7	70.6	12.1	1.23	6.66	0.90	59.2	5.38	–	8.61	2.72
		max	3.50	–	–	13,600	8530	2090	2540	77.4	1030	35.3	51.9	414	11.7	59.2	28.1	–	210	486
		mean	3.50	–	–	11,800	3280	636	1320	47.0	458	24.3	14.6	94.2	6.31	59.2	12.6	–	57.1	88.5
		N	28	–	–	28	27	4	3	2	4	4	23	28	2	1	5	–	18	13
Stage III	17LL13A	minimum	3.45	–	–	6850	600	519	1140	42.1	117	40.9	7.29	15.6	–	–	17.6	–	50.7	17.6
		max	3.45	–	–	12,600	11,400	603	2230	101	1170	55.1	24.1	635	–	–	18.2	–	734	725
		mean	3.45	–	–	10,600	4590	561	1560	71.4	561	48.0	14.4	195	–	–	17.9	–	195	221
		N	13	–	–	13	13	2	3	2	7	2	7	12	–	–	2	–	7	10
	17LL13B	minimum	1.03	36.6	–	3980	855	62.7	7800	23.4	108	20.9	5.13	9.92	–	19.2	11.6	1.72	36.5	2.73
		max	4.69	236	–	16,400	11,400	62.7	7800	142	305	20.9	42.4	298	–	93.5	15.3	4.14	323	130
		mean	3.34	136	–	10,500	3660	62.7	7800	75.5	174	20.9	15.2	85.5	–	56.4	13.3	2.67	130	28.1
		N	16	2	–	16	14	1	1	6	5	1	9	14	–	2	3	5	7	10
	17LL13C	minimum	3.45	–	–	9620	453	27.6	62.3	6.69	23.0	25.5	6.13	15.3	0.99	–	1.86	–	18.7	2.01
		max	3.45	–	–	13,500	6680	391	2490	40.3	378	182	29.2	675	1.73	–	28.1	–	248	278
		mean	3.45	–	–	12,100	2570	204	1080	20.0	170	81.0	11.9	137	1.36	–	13.6	–	81.0	59.4
		N	29	–	–	29	25	3	6	7	11	4	22	29	2	–	5	–	21	18
Stage IV	17LL15A	minimum	3.38	80.7	260	12,500	1360	–	–	–	–	–	16.7	36.6	–	818	56.8	2.44	20.0	27.6
		max	7.81	319	725	29,400	6650	–	–	–	–	–	31.2	476	–	818	56.8	8.31	245	92.5
		mean	5.50	168	450	21,200	3220	–	–	–	–	–	24.5	156	–	818	56.8	6.25	114	63.3
		N	14	4	3	14	11	–	–	–	–	–	8	14	–	1	1	4	5	7

Notes: Salinities (wt% NaCl$_{eqv.}$ used as internal standard for LA–ICP–MS quantification) underlined represent the average values estimated from a group of fluid inclusions while the others were obtained from individual fluid inclusions for "one to one" LA–ICP–MS quantification; "–" = below the detection limit or not quantifiable; N = number of the results above detection limit.
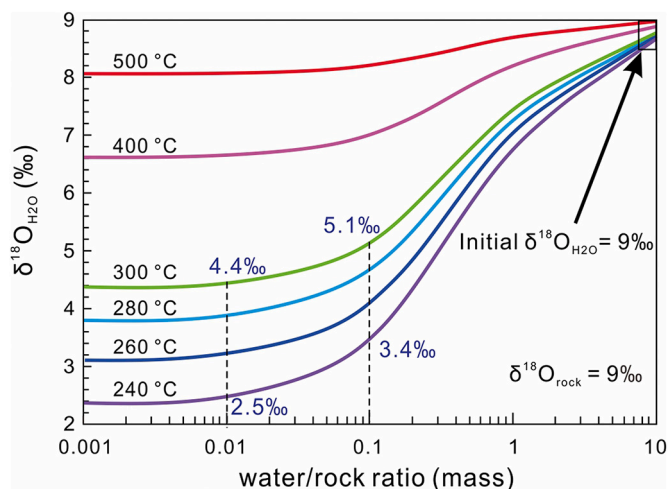
Fig. 14. Modelling for oxygen isotopic exchange between ore-forming fluids and granitic wallrocks as the function of water/rock ratio and equilibration temperature. The modelling is based on the method of Taylor (1974). See text for more details.

rarely occurs in the studied deposits.

The low salinities and moderate to low Th_{tot} of the fluid inclusions in the studied deposits are different from those in the intrusion-associated deposits (e.g. the porphyry and skarn deposits) (Fig. 15a). All the orogenic, epithermal and Carlin-type gold deposits commonly have low Th_{tot} and salinities, but the significant enrichment of CO_2 in the studied deposits can differ from the epithermal and Carlin-type gold deposits (Fig. 15b). The epithermal and Carlin-type gold deposits typically have Th_{tot} values lower than 300 °C (Simmons et al., 2005; Cline, 2018), which are also lower than those of the studied deposits (Fig. 15a; Table 4). In conclusion, the salinities, temperatures and CO_2 contents of the studied fluid inclusions match well with those of the orogenic gold deposits.

The elemental compositions of fluid inclusions plotted in the binary diagrams of K/Na vs. Rb/Na, K/Na vs. Cs/Na, K/Na vs. Cu/Na and K/Na vs. Sr/Na and the ternary diagrams of Rb–Sr–Cs, K–Na–Cu, K–Na–Rb and K–Na–Sr indicate that the fluids in the studied deposits differ from the MVT, magmatic–hydrothermal and low-grade (greenschist facies) metamorphic fluids (Figs. 16 and 17), but are similar to the metamorphic fluids derived from moderate-grade metamorphism (amphibolite facies). An orogenic gold deposit derived from greenschist- to amphibolite-facies metamorphism was also used for comparison. The results shows that the studied fluid inclusions plot closely to the above orogenic gold deposit in most used diagrams (Figs. 16 and 17).

In summary, all the above results indicate that the ore-forming fluids of the studied deposits resemble those of the orogenic deposits, which were probably generated through prograde metamorphic devolatilization.

5.5. Generation of the auriferous fluids and genetic model

The conventional genetic model proposed for orogenic gold deposits invokes the devolatilization of crustal rocks at greenschist- to amphibolite-facies metamorphism (Goldfarb et al., 2005; Tomkins and Grundy, 2009; Phillips and Powell, 2010). This seems to be unfeasible for the Jiaodong gold deposits because the Jiaodong Peninsula experienced crustal extension during the Early Cretaceous with no regional metamorphism being temporally and spatially associated with these deposits. An improved orogenic model proposed recently for the Jiaodong gold deposits suggests that the ore-forming fluids were derived from the dehydration of oceanic lithosphere and the overlying sediments of the subducting Paleo-Pacific slab (Goldfarb and Santosh, 2014; Groves and Santosh, 2016). However, this raises several questions including how the ore-forming fluids could have passed through the thick mantle wedge and why the large-scale gold mineralization is concentrated in the Jiaodong Peninsula. The Paleo-Pacific (or Izanagi) plate subducted beneath the eastern Asian during the Mesozoic, the trench of which was located at least >1000 km away from the Jiaodong Peninsula (Maruyama et al., 1997; Sun et al., 2007; Kusky et al., 2014). The rollback of the above plate began at ~145 Ma and led to the formation of a big mantle wedge before 125 Ma beneath the eastern NCC

Table 4

Comparisons of geological features between the Jiaodong gold deposits and other types of hydrothermal gold deposits.

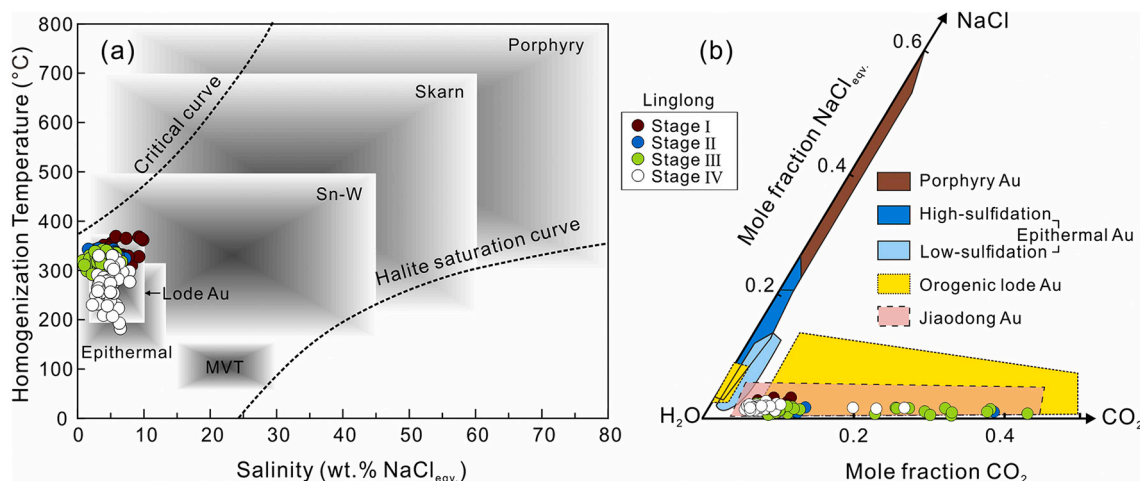|	Jiaodong gold deposits	Orogenic gold deposits	Epithermal gold deposits	Carlin-type gold deposits
Tectonic setting	Cratonic margin; veins typically controlled by faults	Continental margin; compressional to transpressional regime; veins typically in metamorphic rocks	Oceanic arc, continental arc, or back arc extension of continental crust; extensional environments, but commonly in compressional regimes	Back-arc extension and thinning of continental crust
Temperature and formation depth	200–400 °C; commonly 5–10 km	200–700 °C; 2–10 km	100–300 °C; surface–2 km	180–240 °C; <~2–3 km
Alteralization type	K-feldspathization, silicification, sericitization and sulfidation with minor other alteration types such as carbonatization. The different types of alteration in Jiaojia-type gold deposit are much stronger than those in the Linglong-type.	Carbonation, sericitization, sulfidation; skarn-like assemblages in higher temperature deposits	Quartz + adularia ± illite ± calcite (low sulfidation); quartz + alunite ± pyrophyllite ± dickite ± kaolinite (high sulfidation)	Dissolution and silicification of carbonate and argillization of silicates
Mineralization style	Quartz–sulfide veins (Linglong-type); disseminated or stochwork ores (Jiaojia-type); native gold associated with pyrite, quartz, sphalerite, and chalcopyrite	Variable; large veins, vein arrays, saddle reefs, replacement of Fe-rich rocks; native gold with fineness of 920 to 940, associated with pyrite and arsenopyrite or in the quartz carbonate veins	Variable; disseminated or stockwork; veins or scattered particles; native gold or telluride such as sylvanite and petzite	Disseminated replacement mineralization; invisible gold or very fine-grained gold in arsenian pyrite or pyrite
Ore-forming fluids	3–10 wt% $NaCl_{eqv.}$, 3–45 mol% CO_2; traces of CH_4	3–10 wt% $NaCl_{eqv.}$, > 5 mol% CO_2; traces of CH_4 and N_2; commonly crustal metamorphic sources	Variable salinity; <3–10 wt% $NaCl_{eqv.}$, abundant H_2S, near-neutral pH conditions (low sulfidation); <5–15 wt% $NaCl_{eqv.}$, abundant sulfuric acid and minor H_2S (high sulfidation); mixture of meteoric water and magmatic fluids	< 7 wt% $NaCl_{eqv.}$, ~2–4 mol % CO_2; magmatic-hydrothermal fluids; acidic

Notes: The above features are mainly summarized from Groves et al. (1998), Qiu et al. (2002), Goldfarb et al. (2005), Simmons et al. (2005), Fan et al. (2007), Cline (2018) and Deng et al. (2020).

Fig. 15. Comparison of fluid inclusions in Th_{tot}–salinity (a) and H_2O–NaCl–CO_2 fractions (b) with other types of ore deposits. (a) and (b) are after Wilkinson (2001) and Ridley and Diamond (2000), respectively. The field of Jiaodong gold deposits in (b) is drawn using the data of Fan et al. (2007), Wen et al. (2015, 2016), Chai et al. (2017), Guo et al. (2017) and Liu et al. (2018). (For interpretation of the references to colour in this figure legend, the reader is referred to the web version of this article.)
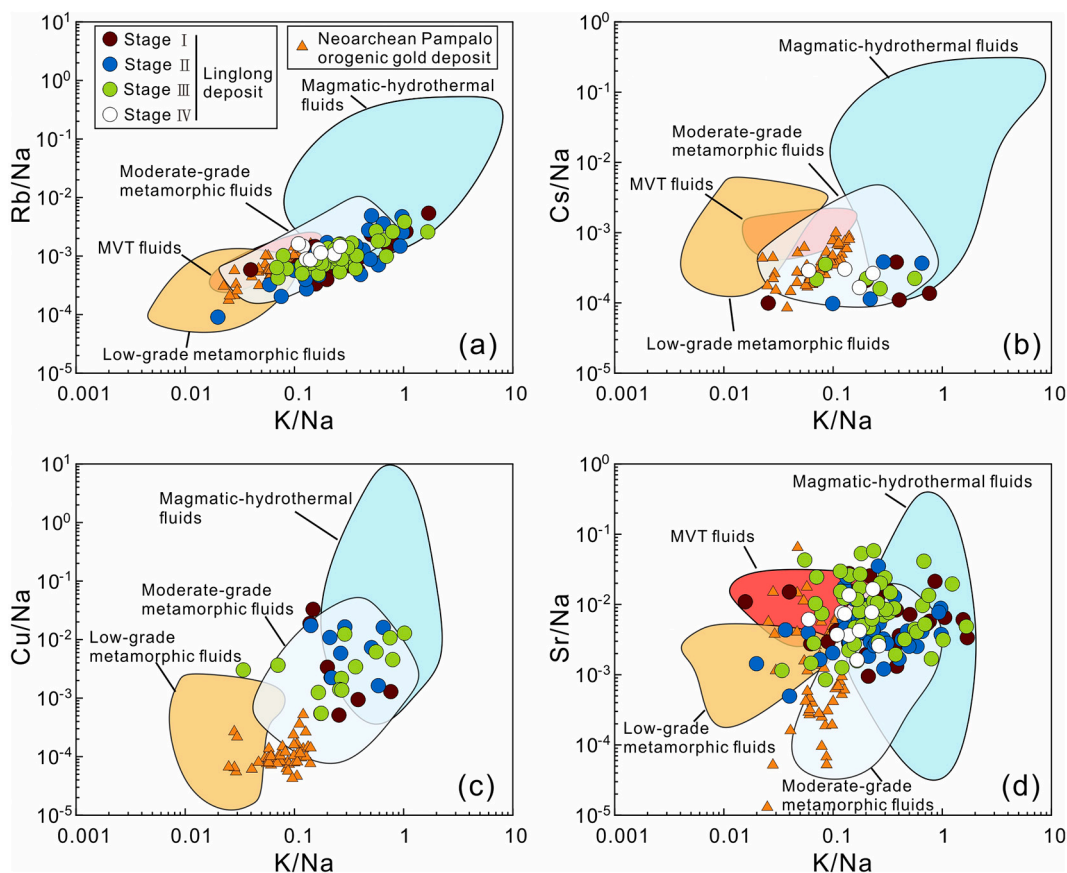
Fig. 16. Comparison of fluid inclusion compositions with different types of fluids and ore deposits in the binary plots of K/Na vs. Rb/Na (a), K/Na vs. Cs/Na (b), K/Na vs. Cu/Na (c) and K/Na vs. Sr/Na (d). The data of magmatic–hydrothermal fluids (represented by the porphyry and skarn deposits) are from Rusk et al. (2004), Klemm et al. (2007), Shu et al. (2017) and Chang et al. (2018), while those of the MVT fluids from Stoffell et al. (2008) and Fusswinkel et al. (2013), low-grade (subgreenschist to lower facies) metamorphic fluids from Marsala et al. (2013) and Miron et al. (2013), moderate-grade (amphibolite facies) metamorphic fluids from Rauchenstein-Martinek et al. (2016) and Neoarchean Pampalo orogenic gold deposit from Fusswinkel et al. (2017). (For interpretation of the references to colour in this figure legend, the reader is referred to the web version of this article.)

(Kusky et al., 2014; Zhu and Sun, 2021). This implies that the ancient mantle wedge during the gold mineralization might have been thicker than 400 km (Xu et al., 2011; Liu et al., 2017). Owing to the great

subduction depth, it is doubtful whether the slab-derived fluids can survive after the long-distance transport. In addition, even if the fluids did succeed in passing through the thick mantle wedge along the deeply-
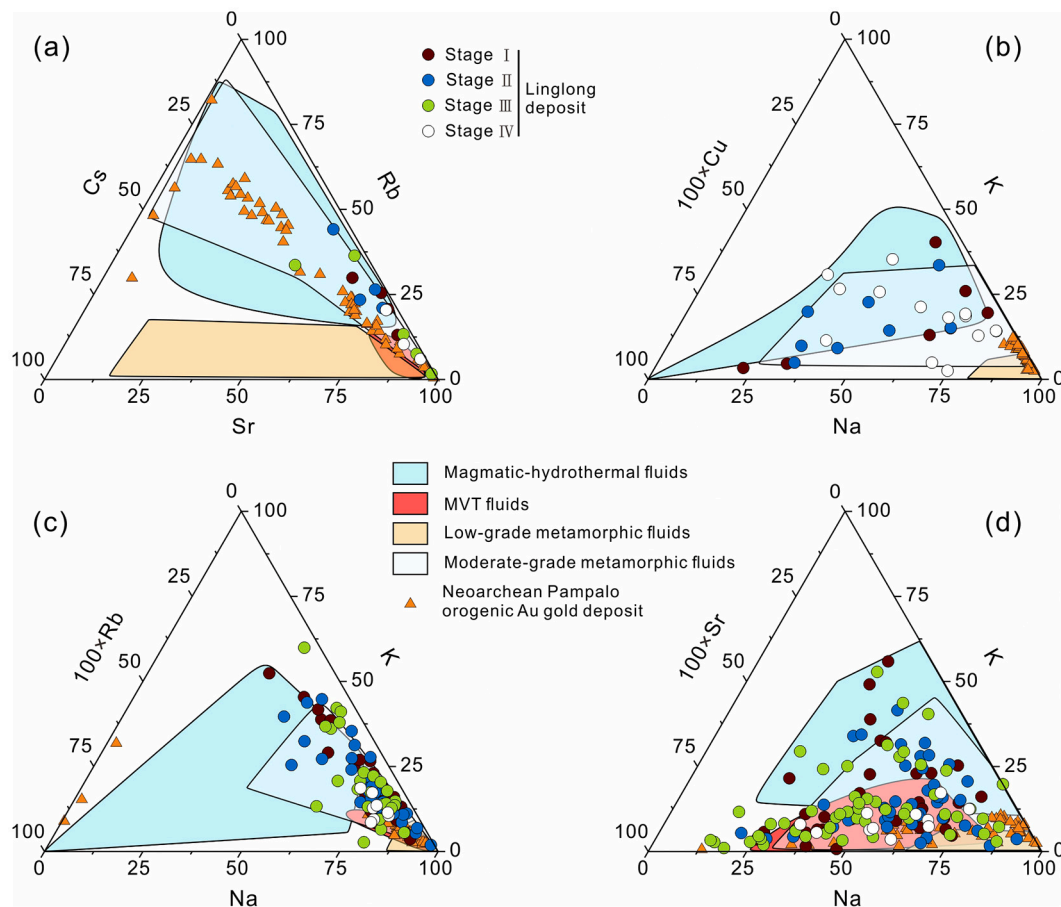
Fig. 17. Comparison of fluid inclusion compositions with different types of fluids and ore deposits in the ternary plots of Sr–Rb–Cs (a), Na–K–100 × Cu (b), Na–K–100 × Rb (c) and Na–K–100 × Sr (d). The sources of data are as those in Fig. 16.

seated faults, it is still difficult to explain why the gold mineralization occurred in the Jiaodong Peninsula during a short time interval, considering that slab dehydration is a long-lasting process and the whole eastern China underwent subduction of the Paleo-Pacific slab during the Mesozoic (Sun et al., 2007; Windley et al., 2010).

The ore-forming fluids of the Jiaodong gold deposits show considerable mantle isotopic features (Mao et al., 2008; Li and Santosh, 2014; Tan et al., 2018; Deng et al., 2020), indicating that their generation might be associated with mantle or mantle-derived rocks. Combined with their metamorphic features (Figs. 15, 16 and 17), it is necessary to evaluate the possibility that the auriferous fluids were generated through moderate- to high-grade metamorphism in the deep crust. It has been suggested that amphibole cumulates favorably form in the lower crust owing to the underplating of hydrous mafic melts, which can act as a fertile source of intracrustal melts and fluids (Davidson et al., 2007). Porphyry Cu—Au deposits generated through partial melting of the amphibole cumulates have been widely identified (e.g., Richards, 2009; Hou et al., 2017), implying that auriferous fluids can be generated through dehydration of the amphibole cumulates if the P-T conditions for partial melting are not reached. Orogenic gold deposits formed through high-grade metamorphism in the deep crust have long been proposed and evaluated (e.g., Cameron, 1989; Cameron et al., 1993; Groves, 1993; Kolb et al., 2015), although there are still some controversies (e.g., Phillips and Powell, 2009; Tomkins, 2013). In the high-grade metamorphism model, the CO_2–H_2O fluids can be generated through amphibolite- to granulite-facies metamorphism (Touret, 2009; Fu and Touret, 2014; Manning, 2018), in which Au is released from the decomposition of Au-bearing sulfides (Cameron, 1989; Cameron et al., 1993). Recent studies on gold mobilization during the metamorphic

devolatilization of volcanic rocks (tholeiitic and calc-alkaline series) show that as much as 59%–77% of the initial Au content can be mobilized during progressive metamorphism to upper amphibolite-facies conditions (>550 °C; Patten et al., 2020). This supports the hypothesis that moderate- to high-grade metamorphism could efficiently mobilize Au from mafic rocks. Large-scale mafic underplating occurred in the lower crust of the eastern NCC during the Late Jurassic to the Early Cretaceous (Liu et al., 2004; Zhang, 2012; Zheng et al., 2012; Ping et al., 2019). These mantle-derived basaltic magmas were enriched in H_2O (Xia et al., 2013) and Au (Wang et al., 2020), facilitating the formation of Au-rich amphibole cumulates. Granulite-facies metamorphism of the above cumulates occurred in the Early Cretaceous (Huang et al., 2004; Liu et al., 2004), which is generally consistent with the timing of the gold mineralization. Remarkable asthenospheric upwelling occurred beneath the eastern NCC due to the rollback of the Paleo-Pacific slab at ~145–125 Ma (Kusky et al., 2014; Zhu and Sun, 2021). This could facilitate the dehydration of the mafic cumulates by heating. In addition, the Pacific plate changed its subduction direction at 125–122 Ma (Sun et al., 2007), leading to the activation of the deeply-seated Tan-Lu fault and its secondary faults (Zhu et al., 2018). This was favorable for the transport of auriferous fluids from deep to shallow depths. Therefore, we propose that the dehydration of amphibole cumulates during amphibolite- to granulite-facies metamorphism in the middle–lower crust was responsible for the generation of the auriferous fluids. This model explains the regionally uniform mineralization along faults, and also matches with the metamorphic properties and mantle isotopic features of the ore-forming fluids.

6. Conclusions

The SEM, LA–ICP–MS and SIMS analyses of quartz show that there are systematic differences in the mineral textures and elemental and isotopic compositions between the different hydrothermal stages, mineralization depths and styles from the studied gold deposits. Combined with the LA–ICP–MS analysis of fluid inclusions, the results lead to the following main conclusions.

(1) In the Linglong-type mineralization, the pH of the ore-forming fluids increased from the pre-mineralization to the ore-forming stages, which was induced by CO_2 degassing during fluid–fluid unmixing, leading to fast Au deposition.

(2) In the Jiaojia-type mineralization, the quartz grains typically show a homogeneous texture with well-correlated lithophile elements (e.g. K, Al and Rb) and low $\delta^{18}O_{quartz}$ values, indicating enhanced fluid–rock interaction that led to Au deposition.

(3) The intensity of fluid–rock interaction increases as the depth increases, leading to decreased $\delta^{18}O_{quartz}$ values. The variable ore-forming processes and fluid–rock interaction complicated the elemental and isotopic systems, indicating that one should be cautious when tracing the real origin of a giant deposit.

(4) The auriferous fluids are metamorphic fluids, which were most likely derived from the devolatilization of previously emplaced H_2O- and Au-rich amphibole cumulates during amphibolite- to granulite-facies metamorphism in the middle–lower crust.

Supplementary data to this article can be found online at https://doi.org/10.1016/j.chemgeo.2022.121027.

Declaration of Competing Interest

The authors declare that they have no known competing financial interests or personal relationships that might influence the work reported in this paper.

Data availability

Data will be made available on request.

Acknowledgements

References

Allan, M.M., Yardley, B.W.D., 2007. Tracking meteoric infiltration into a magmatic-hydrothermal system: a cathodoluminescence, oxygen isotope and trace element study of quartz from Mt. Leyshon, Australia. Chem. Geol. 240, 343–360.

Allan, M.M., Yardley, B.W.D., Forbes, L.J., Shmulovich, K.I., Banks, D.A., Shepherd, T.J., 2005. Validation of LA-ICP-MS fluid inclusion analysis with synthetic fluid inclusions. Am. Mineral. 90, 1767–1775.

Audétat, A., Garbe-Schoenberg, D., Kronz, A., Pettke, T., Rusk, B., Donovan, J.J., Lowers, H.A., 2015. Characterisation of a natural quartz crystal as reference material for microanalytical determination of Ti, Al, Li, Fe, Mn, Ga and Ge. Geostand. Geoanal. Res. 39, 171–184.

Bakker, R.J., Dubessy, J., Cathelineau, M., 1996. Improvements in clathrate modelling: I. The H2O–CO2 system with various salts. Geochim. Cosmochim. Acta 60, 1657–1681.

Barker, S.L.L., Cox, S.F., 2011. Oscillatory zoning and trace element incorporation in hydrothermal minerals: insights from calcite growth experiments. Geofluids 11, 48–56.

Cameron, E.M., 1989. Scouring of gold from the lower crust. Geology 17, 26–29.

Cameron, E.M., Cogulu, E.H., Stirling, J., 1993. Mobilization of gold in the deep crust: evidence from mafic intrusions in the Bamble belt, Norway. Lithos 30, 151–166.

Chai, P., Hou, Z.Q., Zhang, Z.Y., 2017. Geology, fluid inclusion and stable isotope constraints on the fluid evolution and resource potential of the Xiadian gold deposit, Jiaodong Peninsula. Resour. Geol. 67, 341–359.

Chang, J., Li, J.W., Audetat, A., 2018. Formation and evolution of multistage magmatic-hydrothermal fluids at the Yulong porphyry Cu-Mo deposit, eastern Tibet: insights from LA-ICP-MS analysis of fluid inclusions. Geochim. Cosmochim. Acta 232, 181–205.

Cline, J.S., 2018. Nevada's Carlin-type gold deposits: What we've learned during the past 10 to 15 years. In: Muntean, J.L. (Ed.), Diversity in Carlin-Style Gold Deposits, Reviews in Economic Geology, vol. 20, pp. 7–37.

Cox, S.F., 2016. Injection-driven swarm seismicity and permeability enhancement: Implications for the dynamics of hydrothermal ore systems in high fluid-flux, overpressured faulting regimes-an invited paper. Econ. Geol. 111, 559–587.

Davidson, J., Turner, S., Handley, H., Macpherson, C., Dosseto, A., 2007. Amphibole "sponge" in arc crust? Geology 35, 787–790.

Deng, J., Liu, X., Wang, Q., Dilek, Y., Liang, Y., 2017. Isotopic characterization and petrogenetic modeling of Early Cretaceous mafic diking-Lithospheric extension in the North China craton, eastern Asia. Geol. Soc. Am. Bull. 129, 1379–1407.

Deng, J., Yang, L., Groves, D.I., Zhang, L., Qiu, K., Wang, Q., 2020. An integrated mineral system model for the gold deposits of the giant Jiaodong province, eastern China. Earth Sci. Rev. 208, 103274.

Diamond, L.W., 2001. Review of the systematics of CO2–H2O fluid inclusions. Lithos 55, 69–99.

Drummond, S.E., Ohmoto, H., 1985. Chemical evolution and mineral deposition in boiling hydrothermal systems. Econ. Geol. 80, 126–147.

Fan, H.R., Hu, F.F., Yang, J.H., Zhai, M.G., 2007. Fluid evolution and large-scale gold metallogeny during Mesozoic tectonic transition in the Jiaodong Peninsula, eastern China. Geol. Soc. Lond., Spec. Publ. 280, 303–316.

Fu, B., Touret, J.L.R., 2014. From granulite fluids to quartz-carbonate megashear zones: the gold rush. Geosci. Front. 5, 747–758.

Fusswinkel, T., Wagner, T., Waelle, M., Wenzel, T., Heinrich, C.A., Markl, G., 2013. Fluid mixing forms basement-hosted Pb-Zn deposits: insight from metal and halogen geochemistry of individual fluid inclusions. Geology 41, 679–682.

Fusswinkel, T., Wagner, T., Sakellaris, G., 2017. Fluid evolution of the Neoarchean Pampalo orogenic gold deposit (E Finland): constraints from LA-ICPMS fluid inclusion microanalysis. Chem. Geol. 450, 96–121.

Goldfarb, R.J., Santosh, M., 2014. The dilemma of the Jiaodong gold deposits: are they unique? Geosci. Front. 5, 139–153.

Goldfarb, R.J., Baker, T., Dubé, B., Groves, D.I., Hart, C.J.R., Gosselin, P., 2005. Distribution, character, and genesis of gold deposits in metamorphic terranes. In: Economic Geology 100th Anniversary Volume, pp. 407–450.

Götte, T., Pettke, T., Ramseyer, K., Koch-Müller, M., Mullis, J., 2011. Cathodoluminescence properties and trace element signature of hydrothermal quartz: a fingerprint of growth dynamics. Am. Mineral. 96, 802–813.

Götze, J., Plötze, M., Graupner, T., Hallbauer, D.K., Bray, C.J., 2004. Trace element incorporation into quartz: a combined study by ICP-MS, electron spin resonance, cathodoluminescence, capillary ion analysis, and gas chromatography. Geochim. Cosmochim. Acta 68, 3741–3759.

Groves, D.I., 1993. The crustal continuum model for late-Archaean lode-gold deposits of the Yilgarn Block, Western Australia. Mineral. Deposita 28, 366–374.

Groves, D.I., Santosh, M., 2016. The giant Jiaodong gold province: the key to a unified model for orogenic gold deposits? Geosci. Front. 7, 409–417.

Groves, D.I., Goldfarb, R.J., Gebre-Mariam, M., Hagemann, S.G., Robert, F., 1998. Orogenic gold deposits: a proposed classification in the context of their crustal distribution and relationship to other gold deposit types. Ore Geol. Rev. 13, 7–27.

Guillong, M., Meier, D.L., Allan, M.M., Heinrich, C.A., Yardley, B.W.D., 2008. SILLS: AMATLAB-based program for the reduction of laser ablation ICP-MS data of homogeneous materials and inclusions. In: Sylvester, P. (Ed.), Laser Ablation ICP-MS in the Earth Sciences: Current Practices and Outstanding Issues, Mineralogical Associationof Canada Short Course Series, vol. 40, pp. 328–333.

Guo, L., Goldfarb, R.J., Wang, Z., Li, R., Chen, B., Li, J., 2017. A comparison of Jiaojia- and Linglong-type gold deposit ore-forming fluids: do they differ? Ore Geol. Rev. 88, 511–533.

Heinrich, C.A., Pettke, T., Halter, W.E., Aigner-Torres, M., Audetat, A., Gunther, D., Hattendorf, B., Bleiner, D., Guillong, M., Horn, I., 2003. Quantitative multi-element analysis of minerals, fluid and melt inclusions by laser-ablation inductively-coupled-plasma mass-spectrometry. Geochim. Cosmochim. Acta 67, 3473–3497.

Hou, Z., Zhou, Y., Wang, R., Zheng, Y., He, W., Zhao, M., Evans, N.J., Weinberg, R.F., 2017. Recycling of metal-fertilized lower continental crust: origin of non-arc Au-rich porphyry deposits at cratonic edges. Geology 45, 563–566.

Huang, X.L., Xu, Y.G., Liu, D.Y., 2004. Geochronology, petrology and geochemistry of the granulite xenoliths from Nushan, east China: implication for a heterogeneous lower crust beneath the Sino-Korean Craton. Geochim. Cosmochim. Acta 68, 127–149.

Kerr, M.J., Hanley, J.J., Kontak, D.J., Morrison, G.G., Petrus, J., Fayek, M., Zajacz, Z., 2018. Evidence of upgrading of gold tenor in an orogenic quartz-carbonate vein system by late magmatic-hydrothermal fluids at the Madrid Deposit, Hope Bay Greenstone Belt, Nunavut, Canada. Geochim. Cosmochim. Acta 241, 180–218.

Klemm, L.M., Pettke, T., Heinbicth, C.A., Campos, E., 2007. Hydrothermal evolution of the El Teniente deposit, Chile: porphyry Cu-Mo ore deposition from low-salinity magmatic fluids. Econ. Geol. 102, 1021–1045.

Kokh, M.A., Akinfiev, N.N., Pokrovski, G.S., Salvi, S., Guillaume, D., 2017. The role of carbon dioxide in the transport and fractionation of metals by geological fluids. Geochim. Cosmochim. Acta 197, 433–466.

Kolb, J., Dziggel, A., Bagas, L., 2015. Hypozonal lode gold deposits: a genetic concept based on a review of the New Consort, Renco, Hutti, Hira Buddini, Navachab, Nevoria and the Granites deposits. Precambrian Res. 262, 20–44.

Kusky, T.M., Windley, B.F., Wang, L., Wang, Z., Li, X., Zhu, P., 2014. Flat slab subduction, trench suction, and craton destruction: comparison of the North China, Wyoming, and Brazilian cratons. Tectonophysics 630, 208–221.

Lan, T., Hu, R., Fan, H., Bi, X., Tang, Y., Zhou, L., Mao, W., Chen, Y., 2017. In-situ analysis of major and trace elements in fluid inclusion and quartz: LA-ICP-MS method and applications to ore deposits. Acta Petrol. Sin. 33, 3239–3262 (in Chinese with English abstract).

Li, D., Duan, Z., 2007. The speciation equilibrium coupling with phase equilibrium in the H_2O-CO_2-NaCl system from 0 to 250 °C, from 0 to 1000 bar, and from 0 to 5 molality of NaCl. Chem. Geol. 244, 730–751.

Li, S.R., Santosh, M., 2014. Metallogeny and craton destruction: records from the North China Craton. Ore Geol. Rev. 56, 376–414.

Li, X.C., Fan, H.R., Santosh, M., Hu, F.F., Yang, K.F., Lan, T.G., 2013. Hydrothermal alteration associated with Mesozoic granite-hosted gold mineralization at the Sanshandao deposit, Jiaodong Gold Province, China. Ore Geol. Rev. 53, 403–421.

Li, L., Santosh, M., Li, S.R., 2015. The 'Jiaodong type' gold deposits: characteristics, origin and prospecting. Ore Geol. Rev. 65, 589–611.

Liu, Y.S., Gao, S., Yuan, H.L., Zhou, L., Liu, X.M., Wang, X.C., Hu, Z.C., Wang, L.S., 2004. U-Pb zircon ages and Nd, Sr, and Pb isotopes of lower crustal xenoliths from North China Craton: insights on evolution of lower continental crust. Chem. Geol. 211, 87–109.

Liu, Y., Hu, Z., Gao, S., Guenther, D., Xu, J., Gao, C., Chen, H., 2008. In situ analysis of major and trace elements of anhydrous minerals by LA-ICP-MS without applying an internal standard. Chem. Geol. 257, 34–43.

Liu, X., Zhao, D., Li, S., Wei, W., 2017. Age of the subducting Pacific slab beneath East Asia and its geodynamic implications. Earth Planet. Sci. Lett. 464, 166–174.

Liu, J., Wang, J., Liu, Y., Tian, J., Li, X., Zhang, H., Somerville, I., 2018. Ore genesis of the Xiadian gold deposit, Jiaodong Peninsula, East China: information from fluid inclusions and mineralization. Geol. J. 53, 77–95.

Manning, C.E., 2018. Fluids of the lower crust: deep is different. Annu. Rev. Earth Planet. Sci. 46, 67–97.

Mao, J., Wang, Y., Li, H., Pirajno, F., Zhang, C., Wang, R., 2008. The relationship of mantle-derived fluids to gold metallogenesis in the Jiaodong Peninsula: evidence from D–O–C–S isotope systematics. Ore Geol. Rev. 33, 361–381.

Mao, W., Rusk, B., Yang, F.C., Zhang, M.J., 2017. Physical and chemical evolution of the Dabaoshan porphyry Mo deposit, South China: insights from fluid inclusions, cathodoluminescence, and trace elements in quartz. Econ. Geol. 112, 889–918.

Marsala, A., Wagner, T., Wälle, M., 2013. Late-metamorphic veins record deep ingression of meteoric water: a LA-ICPMS fluid inclusion study from the fold-and-thrust belt of the Rhenish Massif, Germany. Chem. Geol. 351, 134–153.

Maruyama, S., Isozaki, Y., Kimura, G., Terabayashi, M., 1997. Paleogeographic maps of the Japanese Islands: plate tectonic synthesis from 750 Ma to the present. Island Arc 6, 121–142.

Maydagán, L., Franchini, M., Rusk, B., Lentz, D.R., McFarlane, C., Impiccini, A., Ríos, F. J., Rey, R., 2015. Porphyry to epithermal transition in the Altar Cu-(Au-Mo) deposit, Argentina, studied by cathodoluminescence, LA-ICP-MS, and fluid inclusion analysis. Econ. Geol. 110, 889–923.

Miron, G.D., Wagner, T., Waelle, M., Heinrich, C.A., 2013. Major and trace-element composition and pressure-temperature evolution of rock-buffered fluids in low-grade accretionary-wedge metasediments, Central Alps. Contrib. Mineral. Petrol. 165, 981–1008.

Mu, L., Hu, R., Bi, X., Tang, Y., Lan, T., Lan, Q., Zhu, J., Peng, J., Oyebamiji, A., 2021. New insights into the origin of the world-class Jinding sediment-hosted Zn-Pb deposit, southwestern China: evidence from LA-ICP-MS analysis of individual fluid inclusions. Econ. Geol. 116, 883–907.

Müller, A., Herrington, R., Armstrong, R., Seltmann, R., Kirwin, D.J., Stenina, N.G., Kronz, A., 2010. Trace elements and cathodoluminescence of quartz in stockwork veins of Mongolian porphyry-style deposits. Mineral. Deposita 45, 707–727.

Patten, C.G.C., Pitcairn, I.K., Molnar, F., Kolb, J., Beaudoin, G., Guilmette, C., Peillod, A., 2020. Gold mobilization during metamorphic devolatilization of Archean and Paleoproterozoic metavolcanic rocks. Geology 48, 1110–1114.

Pettke, T., Oberli, F., Audétat, A., Guillong, M., Simon, A.C., Hanley, J.J., Klemm, L.M., 2012. Recent developments in element concentration and isotope ratio analysis of individual fluid inclusions by laser ablation single and multiple collector ICP-MS. Ore Geol. Rev. 44, 10–38.

Phillips, G.N., Evans, K.A., 2004. Role of CO_2 in the formation of gold deposits. Nature 429, 860–863.

Phillips, G.N., Powell, R., 2009. Formation of gold deposits: review and evaluation of the continuum model. Earth Sci. Rev. 94, 1–21.

Phillips, G.N., Powell, R., 2010. Formation of gold deposits: a metamorphic devolatilization model. J. Metamorph. Geol. 28, 689–718.

Ping, X., Zheng, J., Xiong, Q., Griffin, W.L., Yu, C., Su, Y., 2019. Downward rejuvenation of the continental lower crust beneath the southeastern North China Craton. Tectonophysics 750, 213–228.

Pokrovski, G.S., Roux, J., Ferlat, G., Jonchiere, R., Seitsonen, A.P., Vuilleumier, R., Hazemann, J.L., 2013. Silver in geological fluids from in situ X-ray absorption spectroscopy and first-principles molecular dynamics. Geochim. Cosmochim. Acta 106, 501–523.

Pokrovski, G.S., Akinfiev, N.N., Borisova, A.Y., Zotov, A.V., Kouzmanov, K., 2014. Gold speciation and transport in geological fluids: insights from experiments and physical-chemical modelling. Geol. Soc. Lond., Spec. Publ. 402, 9–70.

Qiu, Y.M., Groves, D.I., McNaughton, N.J., Wang, L.G., Zhou, T.H., 2002. Nature, age, and tectonic setting of granitoid-hosted, orogenic gold deposits of the Jiaodong Peninsula, eastern North China craton, China. Mineral. Deposita 37, 283–305.

Ramboz, C., Pichavant, M., Weisbrod, A., 1982. Fluid immiscibility in natural processes: use and misuse of fluid inclusion data: II. Interpretation of fluid inclusion data in terms of immiscibility. Chem. Geol. 37, 29–48.

Rauchenstein-Martinek, K., Wagner, T., Walle, M., Heinrich, C.A., Arlt, T., 2016. Chemical evolution of metamorphic fluids in the Central Alps, Switzerland: insight from LA-ICPMS analysis of fluid inclusions. Geofluids 16, 877–908.

Reed, M.H., Palandri, J., 2006. Sulfide mineral precipitation from hydrothermal fluids. Rev. Mineral. Geochem. 61, 609–631.

Richards, J.P., 2009. Postsubduction porphyry Cu-Au and epithermal Au deposits: products of remelting of subduction-modified lithosphere. Geology 37, 247–250.

Ridley, J.R., Diamond, L.W., 2000. Fluid chemistry of orogenic lode gold deposits and implications for genetic models. Rev. Econ. Geol. 13, 141–162.

Rottier, B., Kouzmanov, K., Casanova, V., Bouvier, A.S., Baumgartner, L.P., Wälle, M., Fontboté, L., 2021. Tracking fluid mixing in epithermal deposits–Insights from in-situ $\delta^{18}O$ and trace element composition of hydrothermal quartz from the giant Cerro de Pasco polymetallic deposit, Peru. Chem. Geol. 576, 120277.

Rusk, B.G., Reed, M.H., Dilles, J.H., Klemm, L.M., Heinrich, C.A., 2004. Compositions of magmatic hydrothermal fluids determined by LA-ICP-MS of fluid inclusions from the porphyry copper-molybdenum deposit at Butte, MT. Chem. Geol. 210, 173–199.

Rusk, B.G., Lowers, H.A., Reed, M.H., 2008. Trace elements in hydrothermal quartz: relationships to cathodoluminescent textures and insights into vein formation. Geology 36, 547–550.

Shu, Q., Chang, Z., Hammerli, J., Lai, Y., Huizenga, J.M., 2017. Composition and evolution of fluids forming the Baivinnuo'er Zn-Ph skarn deposit, northeastern China: insights from laser ablation ICP-MS study of fluid inclusions. Econ. Geol. 112, 1441–1460.

Simmons, S., White, N., John, D., 2005. Geological characteristics of epithermal precious and basesmetal deposits. In: Economic Geology 100th Anniversary Volume, pp. 485–522.

Steele-MacInnis, M., 2018. Fluid inclusions in the system $H_2O-NaCl-CO_2$: an algorithm to determine composition, density and isochore. Chem. Geol. 498, 31–44.

Stoffell, B., Appold, M.S., Wilkinson, J.J., McClean, N.A., Jeffries, T.E., 2008. Geochemistry and evolution of Mississippi Valley-type mineralizing brines from the Tri-State and Northern Arkansas districts determined by LA-ICP-MS microanalysis of fluid inclusions. Econ. Geol. 103, 1411–1435.

Sun, W., Ding, X., Hu, Y.H., Li, X.H., 2007. The golden transformation of the Cretaceous plate subduction in the west Pacific. Earth Planet. Sci. Lett. 262, 533–542.

Tan, J., Wei, J., He, H., Su, F., Li, Y., Fu, L., Zhao, S., Xiao, G., Zhang, F., Xu, J., Liu, Y., Stuart, F.M., Zhu, R., 2018. Noble gases in pyrites from the Guocheng-Liaoshan gold belt in the Jiaodong province: evidence for a mantle source of gold. Chem. Geol. 480, 105–115.

Tang, G.Q., Liu, Y., Li, Q.L., Feng, L.J., Wei, G.J., Su, W., Li, Y., Ren, G.H., Li, X.H., 2020. New natural and fused quartz reference materials for oxygen isotope microanalysis. At. Spectrosc. 41, 188–193.

Taylor, J.H.P., 1974. The application of oxygen and hydrogen isotope studies to problems of hydrothermal alteration and ore deposition. Econ. Geol. 69, 843–883.

Tomkins, A.G., 2013. On the source of orogenic gold. Geology 41, 1255–1256.

Tomkins, A.G., Grundy, C., 2009. Upper temperature limits of orogenic gold deposit formation: constraints from the granulite-hosted Griffin's Find Deposit, Yilgarn Craton. Econ. Geol. 104, 669–685.

Touret, J.L.R., 2009. Mantle to lower-crust fluid/melt transfer through granulite metamorphism. Russ. Geol. Geophys. 50, 1052–1062.

Truche, L., Bazarkina, E.F., Berger, G., Caumon, M.C., Bessaque, G., Dubessy, J., 2016. Direct measurement of CO_2 solubility and pH in NaCl hydrothermal solutions by combining in-situ potentiometry and Raman spectroscopy up to 280 °C and 150 bar. Geochim. Cosmochim. Acta 177, 238–253.

Wagner, T., Fusswinkel, T., Walle, M., Heinrich, C.A., 2016. Microanalysis of fluid inclusions in crustal hydrothermal systems using laser ablation methods. Elements 12, 323–328.

Wang, H., Chen, J., Wang, Y., Ding, K., 1989. Geochemical studies of Au-bearing formation in Jiaodong Peninsula,Shandong province. Acta Geochim. 8, 213–227.

Wang, X., Chou, I.M., Hu, W., Burruss, R.C., Sun, Q., Song, Y., 2011. Raman spectroscopic measurements of CO_2 density: experimental calibration with high-pressure optical cell (HPOC) and fused silica capillary capsule (FSCC) with application to fluid inclusion observations. Geochim. Cosmochim. Acta 75, 4080–4093.

Wang, Z., Cheng, H., Zong, K., Geng, X., Liu, Y., Yang, J., Wu, F., Becker, H., Foley, S., Wang, C.Y., 2020. Metasomatized lithospheric mantle for Mesozoic giant gold deposits in the North China craton. Geology 48, 169–173.

Weatherley, D.K., Henley, R.W., 2013. Flash vapourization during earthquakes evidenced by gold deposits. Nat. Geosci. 6, 294–298.

Wen, B.J., Fan, H.R., Santosh, M., Hu, F.F., Pirajno, F., Yang, K.F., 2015. Genesis of two different types of gold mineralization in the Linglong gold field, China: constrains from geology, fluid inclusions and stable isotope. Ore Geol. Rev. 65, 643–658.

Wen, B.J., Fan, H.R., Hu, F.F., Liu, X., Yang, K.F., Sun, Z.F., Sun, Z.F., 2016. Fluid evolution and ore genesis of the giant Sanshandao gold deposit, Jiaodong gold province, China: constrains from geology, fluid inclusions and H-O-S-He-Ar isotopic compositions. J. Geochem. Explor. 171, 96–112.

Wilkinson, J.J., 2001. Fluid inclusions in hydrothermal ore deposits. Lithos 55, 229–272.

Williams-Jones, A.E., Bowell, R.J., Migdisov, A.A., 2009. Gold in solution. Elements 5, 281–287.

Windley, B.F., Maruyama, S., Xiao, W.J., 2010. Delamination/thinning of sub-continental lithospheric mantle under Eastern China: the role of water and multiple subduction. Am. J. Sci. 310, 1250–1293.

Xia, Q., Liu, J., Liu, S., Kovacs, I., Feng, M., Dang, L., 2013. High water content in Mesozoic primitive basalts of the North China Craton and implications on the destruction of cratonic mantle lithosphere. Earth Planet. Sci. Lett. 361, 85–97.

Xiong, L., Zhao, X., Wei, J., Jin, X., Fu, L., Lin, Z., 2020. Linking Mesozoic lode gold deposits to metal-fertilized lower continental crust in the North China Craton: evidence from Pb isotope systematics. Chem. Geol. 533, 119440.

Xu, W., Zheng, T., Zhao, L., 2011. Mantle dynamics of the reactivating North China Craton: constraints from the topographies of the 410-km and 660-km discontinuities. Sci. China Earth Sci. 54, 881–887.

Yan, Y., Zhang, N., Li, S., Li, Y., 2014. Mineral chemistry and isotope geochemistry of pyrite from the Heilangou gold deposit, Jiaodong Peninsula, Eastern China. Geosci. Front. 5, 205–213.

Zhang, H.F., 2012. Destruction of ancient lower crust through magma underplating beneath Jiaodong Peninsula, North China Craton: U–Pb and Hf isotopic evidence from granulite xenoliths. Gondwana Res. 21, 281–292.

Zhang, L., Liu, J., Zhou, H., Chen, Z., 1989. Oxygen isotope fractionation in the quartz-water-salt system. Econ. Geol. 84, 1643–1650.

Zhang, L., Weinberg, R.F., Yang, L., Groves, D.I., Sai, S., Matchan, E., Phillips, D., Kohn, B.P., Miggins, D.P., Liu, Y., Deng, J., 2020. Mesozoic orogenic gold mineralization in the Jiaodong Peninsula, China: a focused event at 120 ± 2 Ma during cooling of pregold granite intrusions. Econ. Geol. 115, 415–441.

Zheng, J.P., Griffin, W.L., Ma, Q., O'Reilly, S.Y., Xiong, Q., Tang, H.Y., Zhao, J.H., Yu, C. M., Su, Y.P., 2012. Accretion and reworking beneath the North China Craton. Lithos 149, 61–78.

Zhu, R., Sun, W., 2021. The big mantle wedge and decratonic gold deposits. Sci. China Earth Sci. 64, 1451–1462.

Zhu, G., Liu, C., Gu, C., Zhang, S., Li, Y., Su, N., Xiao, S., 2018. Oceanic plate subduction history in the western Pacific Ocean: constraint from late Mesozoic evolution of the Tan-Lu Fault Zone. Sci. China Earth Sci. 61, 386–405.